Unveiling the 100 pc scale nuclear radio structure of NGC 6217 with e-MERLIN and the VLA

D. R. A. Williams [1,2]⋆ I. M. McHardy,[1] R. D. Baldi [1] R. J. Beswick,[3] M. Pahari [1]
M. K. Argo [3,4] A. Beri,[1,5] P. Boorman,[1] E. Brinks,[6] B. T. Dullo,[7,8,9] D. M. Fenech,[10]
J. Ineson,[1] P. Kharb [11] J. H. Knapen,[8,9,12] T. W. B. Muxlow[3] and J. Westcott [6]

[1]_School of Physics and Astronomy, University of Southampton, Southampton SO17 1BJ, UK_
[2]_Department of Physics, University of Oxford, Denys Wilkinson Building, Keble Road, Oxford OX1 3RH, UK_
[3]_Jodrell Bank Centre for Astrophysics, School of Physics and Astronomy, The University of Manchester, Manchester M13 9PL, UK_
[4]_Jeremiah Horrocks Institute, University of Central Lancashire, Preston, Lancashire PR1 2HE, UK_
[5]_DST-INSPIRE Faculty, Indian Institute of Science Education and Research (IISER), Mohali, Punjab 140306, India_
[6]_Centre for Astrophysics Research, University of Hertfordshire, College Lane, Hatfield AL10 9AB, UK_
[7]_Departamento de Astrofísica y Ciencias de la Atmósfera, Universidad Complutense de Madrid, E-28040 Madrid, Spain_
[8]_Instituto de Astrofísica de Canarias, Vía Láctea S/N, E-38205 La Laguna, Spain_
[9]_Departamento de Astrofísica, Universidad de La Laguna, E-38206 La Laguna, Spain_
[10]_Astrophysics Group, Cavendish Laboratory, University of Cambridge, CB3 0HE, UK_
[11]_National Centre for Radio Astrophysics – Tata Institute of Fundamental Research, Pune University Campus, Post Bag 3, Ganeshkhind, Pune 411007, India_
[12]_Astrophysics Research Institute, Liverpool John Moores University, IC2, Liverpool Science Park, 146 Brownlow Hill, Liverpool L3 5RF, UK_

ABSTRACT

We present high-sensitivity 1.51 GHz e-MERLIN (e-Multi-Element Radio-Linked Interferometer Network) radio images of the nearby galaxy NGC 6217. We resolve the compact radio source at the centre of NGC 6217 for the first time, finding a twin-lobed structure with a total linear size of ∼4 arcsec (∼400 pc). The radio source does not have a compact central core, but there is an unresolved hotspot near the outer edge of the southern lobe. Combining our e-MERLIN data with new VLA (Very Large Array) A-Array data and archival multiwavelength data, we explore possible scenarios which might explain this complex radio morphology. We conclude that this radio source is most likely powered by a low-luminosity active galactic nucleus but with a possible important contribution from nuclear star formation. We also investigate the origin of a putative X-ray jet in NGC 6217, previously suggested in the literature. This 'jet' consists of three X-ray 'knots' in a line, pointed away from the nucleus, with a total size of ∼3 arcmin (∼15 kpc). We find no extended radio emission coincident with the 'jet'. An additional compact radio source, aligned with the knots but without an X-ray counterpart is detected. We detect infrared/optical sources falling within the X-ray extraction regions of the 'knots', but note that these sources could be chance associations due to high source density around the target field and we estimate the probability of three randomly aligned X-ray sources to be 0.3 per cent in this field.

Key words: galaxies: active – galaxies: jets – radio continuum: galaxies – X-rays: galaxies.

1 INTRODUCTION

Active galactic nuclei (AGNs), such as quasars and radio galaxies, can exhibit powerful collimated radio jets on scales of ∼100 kpc (e.g. Bagchi et al. 2007; Hocuk & Barthel 2010). Some low-luminosity AGN (LLAGN) can host small, kpc-scale radio jets

or bubbles (Elmouttie et al. 1995; Irwin & Saikia 2003; Hota & Saikia 2006; Kharb et al. 2006, 2010; Nyland et al. 2017; Capetti, Massaro & Baldi 2017; Panessa et al. 2019) but when identifying these regions, caution must be taken to remove any contamination from star formation (SF) regions, supernovae (SNe), and starburst super winds (Pedlar, Unger & Dyson 1985; Baum et al. 1993; Heckman, Lehnert & Armus 1993; Colbert et al. 1996; Baldi et al. 2018a; Ho & Ulvestad 2001; Ramírez-Olivencia et al. 2018; Panessa et al. 2019). While the radio jets in AGN have been studied for

decades, the presence of cospatial X-ray emission is a more recent discovery (Tavecchio et al. 2000; Schwartz et al. 2000; Chartas et al. 2000; Celotti, Ghisellini & Chiaberge 2001; Sambruna et al. 2001; Harris & Krawczynski 2006; Worrall 2009). However, there are very few objects near enough to spatially resolve these X-ray jets, so new candidates for radio/X-ray/optical follow-up are useful; for example, 3C 273 (Sambruna et al. 2001; Jester et al. 2005; Harris et al. 2017), M 87 (Marshall et al. 2002; Wilson & Yang 2002), and Centaurus A (Kraft et al. 2002; Hardcastle et al. 2003) are just three objects which can be resolved, but are all radio-loud sources, defined as the ratio of radio and optical luminosities, $L_{\mathrm{radio}}/L_{\mathrm{optical}} > 10$ (Kellermann et al. 1989), but see also (e.g. Terashima & Wilson 2003; Cirasuolo et al. 2003; Capetti & Balmaverde 2010; Kharb et al. 2012; Bonzini et al. 2013; Padovani 2017; Padovani et al. 2017; Panessa et al. 2019).

One potential object for resolving and studying low-powered X-ray jets is the barred spiral galaxy NGC 6217. Pietsch & Arp (2001, hereafter PA01) compared radio images of NGC 6217 from the NRAO VLA Sky Survey (NVSS; Condon 1987) with *ROSAT* X-ray contour plots and claimed an extension south-west of the nucleus of NGC 6217 that was aligned in both wavebands. PA01 hence concluded that it was possible that the X-rays could form the base of a radio jet. However, with the resolution of the VLA (the NSF Karl G. Jansky Very Large Array for the NVSS in D/DnC arrays) and *ROSAT* being 45 arcsec (at 1.4 GHz) and ~25 arcsec (at 1 keV) respectively, neither observation was capable of adequately resolving any jets in NGC 6217. More recently, Falocco, Larsson & Nandi (2017, hereafter F17), analysed *XMM–Newton*[1] images and spectra of NGC 6217, obtained in 2001, 2002, and 2007, and reported on the alignment of three X-ray 'knots' and hence a 'likely' X-ray jet emanating from the core in a south-west direction extending over 3 arcmin. They supported the original PA01 assertion from the poorer angular resolution X-ray data. However, both PA01 and F17 used the same NVSS images of NGC 6217. Higher resolution radio data from subarcsecond resolution radio interferometers are required to analyse the radio emission in the putative X-ray jet in this galaxy. Hence, interferometers like e-MERLIN (e-Multi-Element Radio-Linked Interferometer Network) and VLA[2] are ideal instruments for the study of the radio emission and the nature of the aligned X-ray knots in NGC 6217.

In the literature, NGC 6217 has not been well observed at radio frequencies other than in surveys with poor angular resolution. The 1465 MHz radio image of NGC 6217 at a resolution of ~15 arcsec from Hummel et al. (1985) shows an elongation along a PA of 160°, emanating from a core. The follow-up survey at lower resolution, ~0.9 arcmin, by Condon (1987) showed only a core with a weak elongation in the south-west (PA ~ 225°), and no symmetrical counterjet or outflow. However, Vila et al. (1990) showed a mostly unresolved source at 1.49 GHz with the VLA in A-array, but with a significant extension to the south-east and north-west along a PA of ~135° and clearly larger than the beam size at 20 cm of 1.5 arcsec × 1.06 arcsec. We therefore used the e-MERLIN interferometer as part of the Legacy e-MERLIN Multi-band Imaging of Nearby Galaxies survey (LeMMINGs; Beswick

---

[1] Based on observations obtained with *XMM–Newton*, an ESA science mission with instruments and contributions directly funded by ESA Member States and NASA.

[2] The National Radio Astronomy Observatory is a facility of the National Science Foundation operated under cooperative agreement by Associated Universities, Inc.

---

et al. 2014) 'deep' sample to take deeper, high-resolution data to directly image the nuclear region at 150 mas scales at 1.51 GHz. We also obtained new VLA-A array images to improve the definition of the arcsecond-scale structure.

The distance to NGC 6217 is listed between ~19 and 35 Mpc (Tully & Fisher 1977; Hummel 1980; Condon et al. 1990; Tutui & Sofue 1997; Pietsch & Arp 2001; Paturel et al. 2003). We adopt the same distance to NGC 6217 as F17 of $z = 0.0045$ (20.1 Mpc with an angular scale of 97 pc arcsec^{-1}, see also Cabrera-Lavers & Garzón 2004). It is of morphological type (R'L)SB(rs)b (Sandage & Tammann 1981; de Vaucouleurs et al. 1991; Buta et al. 2015) i.e. a barred spiral galaxy with an inner and outer (pseudo-) ring structure and with an SF rate of ~2.9 M$_\odot$ yr^{-1} (James et al. 2004; Knapen & James 2009). Different authors classify the nuclear region in NGC 6217 variably as a Seyfert 2 (Cabrera-Lavers & Garzón 2004), H II Region (Ho, Filippenko & Sargent 1997a; Véron-Cetty & Véron 2006) or a LINER (low-ionization nuclear emission-line region, Nicholson, Mittaz & Mason 1997; Falocco et al. 2017). The exact nuclear classification is important for understanding the ionization mechanisms in the nucleus: Seyferts are ionized by an AGN, whereas H II regions are ionized through SF processes. On the other hand, LINERs are thought to be ionized by post-asymptotic giant branch stars, LLAGN or shocks, (Heckman 1980; Halpern & Steiner 1983; Ferland & Netzer 1983; Terlevich & Melnick 1985; Capetti & Baldi 2011; Singh et al. 2013). The mass of the black hole (BH) in NGC 6217 is estimated from the M–σ relation (Magorrian et al. 1998; Ferrarese & Merritt 2000) by using the stellar velocity dispersion of NGC 6217 from Ho et al. (1997b) and using the M–σ relation of Woo & Urry (2002) to obtain a BH mass of 2.0×10^6 M$_\odot$.

The purpose of this paper is twofold: to investigate the nature of the nuclear emission in NGC 6217 and to check if radio emission in the galaxy spatially is coincident with the X-ray jet suggested by PA01 and F17. This paper is structured as follows: we describe the observations and data reduction in Section 2, in Section 3, we show the resulting radio images and compare these to other ancillary wavelength data and we discuss our spectral energy distributions (SEDs) and X-ray fitting techniques. In Section 4, we discuss the results and, finally, in Section 5, we summarize and present our conclusions. We adopt the following cosmology for computing luminosity distances: $H_0 = 67.3$ km s^{-1} Mpc^{-1}, $\Omega_\Lambda = 0.685$, and $\Omega_M = 0.315$ (Planck Collaboration et al. 2014).

2 OBSERVATIONS AND DATA REDUCTION

Here, we discuss the main data sources relevant to this paper: the recently acquired full-resolution 1.51 GHz e-MERLIN, and VLA data, *XMM–Newton*, and other ancillary wavelength data.

2.1 Radio data reduction and imaging

2.1.1 e-MERLIN

The e-MERLIN *L*-band (1.51 GHz) observations of NGC 6217 were obtained as part of the LeMMINGs survey (Beswick et al. 2014; Baldi et al. 2018a). LeMMINGs is a statistically complete radio survey of all the galaxies in the Palomar spectroscopic bright galaxy sample (Filippenko & Sargent 1985; Ho, Filippenko & Sargent 1995; Ho et al. 1997a,b,c; Ho, Filippenko & Sargent 1997d,e, 2003; Ho et al. 2009) of $\delta \geq 20°$. The observations were made as part of the 'deep' part of the LeMMINGs sample, which constitutes six objects of scientific interest, observed at a greater depth than the 'shallow' sample and with a fully sampled *uv*-plane: M 82 (Muxlow

et al. [2010]), IC 10 (Westcott et al. [2017]), NGC 4151 (Williams et al. [2017]), NGC 5322 (Dullo et al. [2018]), M 51b (Rampadarath et al. [2018]), and NGC 6217 (this paper). The data were obtained on 2016 April 7 with all seven antennas, including the Lovell Telescope, participating in the observing run and 21 h on-source time (see Table [1]). The calibrator J1723+7653 (J172359.4+765312) was used for phase referencing and OQ208 and 3C 286 were used as the bandpass and flux calibrators, respectively. The target was observed for ∼12.5 min, alternating with a ∼2 min observation of the phase calibrator. The flux and bandpass calibrators were observed near the beginning of the run. The *uv*-plane coverage of e-MERLIN and VLA data made with the CASA e-MERLIN pipeline[3] is shown in Fig. [1] (see the next section for the VLA data overview).

The data were correlated and averaged at Jodrell Bank first before they were flagged with the SERPent (Peck & Fenech [2013]) flagging code to excise the worst cases of radio frequency interference (RFI) from the data before calibration could begin. The AIPS (Wells [1985]) tasks SPFLG and IBLED allowed for manual inspection of the data to further flag low-level RFI. The observation was centred on 1.51 GHz, using a total bandwidth of 512 MHz in eight intermediate frequencies (IFs) of 64 MHz each. In addition to RFI flagging, channels at the ends of each IF and the band were flagged as they showed no coherent phase, as were the first two IFs on all Lovell LL-polarization baselines, due to the inclusion of a test filter.

The procedure outlined in the e-MERLIN cookbook (Belles et al. [2015]) was used to calibrate the data, fitting fringes with AIPS task FRING, phase calibrating, and then applying gain corrections to the antennas. The bandpass solutions were found and subsequently applied to the data, before imaging and self-calibration of the phase calibrator. Erroneous data points were flagged out at each part of the process before the calibration files were applied.

After initial calibration in AIPS, the e-MERLIN data were imaged using IMAGR and self-calibrated. On all baselines, IF 1 and 2 had a very poor signal-to-noise ratio due to RFI, hence, large parts of these bands were removed before producing final images. Other bright sources of emission in a radius of a few arcminutes from the core of NGC 6217 were also imaged to improve the image fidelity and so that their side lobes could be removed from the final image of NGC 6217. The images were naturally weighted to achieve the best signal-to-noise ratio. The data were reweighted using REWAY, thus increasing the weighting given to the Lovell antenna which is larger and more sensitive, and which further improved the signal-to-noise ratio. Further self-calibration followed and the final image was created when the noise in the image reached 7 μJy. While initial images were made in AIPS, further image making was processed in CASA (McMullin et al. [2007]).

2.1.2 VLA-A Array data

NGC 6217 was observed with the VLA in A configuration on 2016 December 16 for 4.3 min centred at 1.51 GHz (*L* band) over a bandwidth of 1.024 GHz in 16 spectral windows of 64 MHz, each in turn with 64 channels (see Table [1]). Standard VLA flagging and calibration routines were performed using version 4.7 of the VLA pipeline in CASA 4.7.[4] The pipeline products were reviewed and additional RFI excision was made where necessary. Due to excessive RFI contamination, spectral window 8 was flagged and
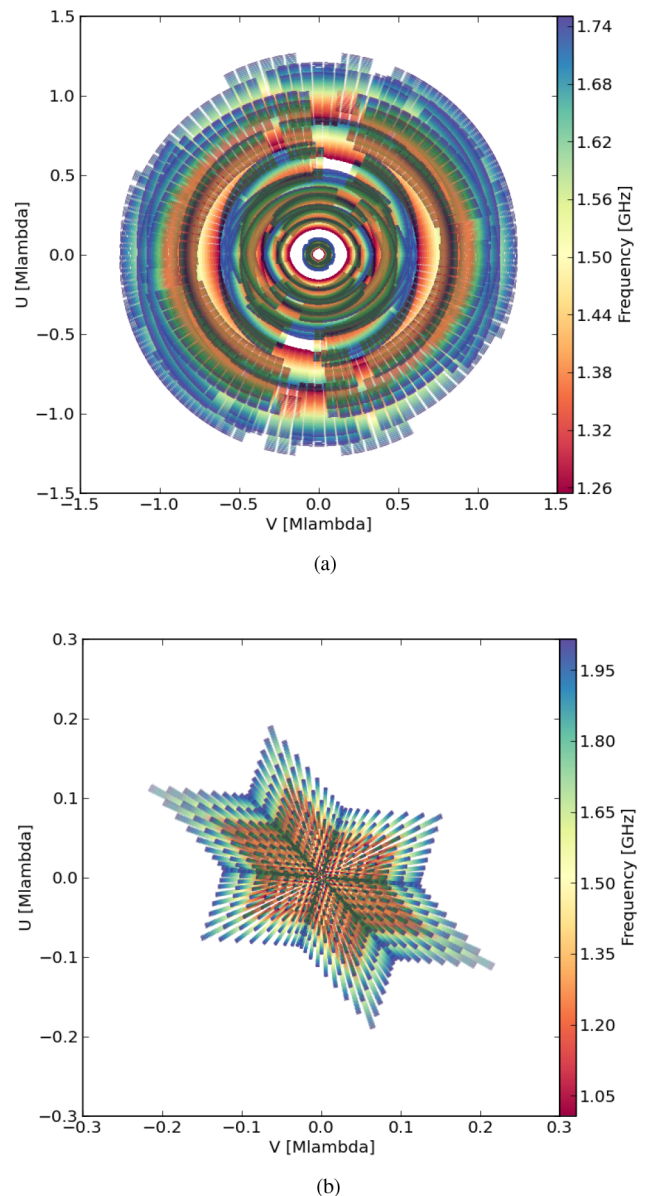
Figure 1. Full observed *uv*-plane of NGC 6217 at 1.51 GHz, using (a) the new LeMMINGs (e-MERLIN) deep data with all seven antennas included and (b) the new VLA A-array data with all antennas.

removed before the final image making procedures. The resulting image achieved an rms of 53 μJy beam⁻¹.

The VLA data were imaged in CASA using CLEAN, first with a large field to help identify the bright sources in the field and then with smaller fields to remove the effects of these contaminating sources of emission from the NGC 6217 image. The data were naturally weighted to ensure good signal-to-noise ratio.

2.1.3 Data combination

After the data were calibrated, we exported the e-MERLIN and VLA data sets to CASA and combined them. First, both data sets were reweighted using the CASA task statwt to reweight each individual visibility by its rms value. Following this step, both data sets were combined and imaged with TCLEAN in CASA

Table 1. Radio data sets of NGC 6217 at different frequencies with different arrays used in this paper. The e-MERLIN and VLA-A Array data sets observed in 2016 were made as part of the LeMMINGs 'deep' sample.

Data	e-MERLIN	VLA
Obs. date (yyyy-mm-dd)	2016-04-07	2016-12-16
Central frequency (GHz)	1.51	1.51
Bandwidth (GHz)	0.512	1.024
Time on source	21 h	4.3 min
Beam size (arcsec × arcsec)	0.15 × 0.15	1.33 × 0.84
Noise level (μJy beam^{-1})	7	53

with clean boxes specified around the core and all radio sources identified from the e-MERLIN and VLA images and a Briggs weighting scheme (`robust = 0`) to image both the compact and diffuse structure. We attempted cleaning with different values of the `multiscale` parameter and the robustness in the Briggs parameter and found the default values of `robust = 0` and `multiscale = [0,5,10]` to give the best compromise between diffuse structure and compact, point-like sources. To properly sample the hybrid point spread function (PSF) of the combined e-MERLIN and VLA data, we oversampled the beam by a factor of 16 (Radcliffe, private communication). This approach allowed us to calculate the correct hybrid PSF which we then used as the `bmaj`, `bmin`, and `bpa` parameters in TCLEAN. We could then image with standard Nyquist sampling while correctly fitting the hybrid PSF.

2.2 *XMM–Newton* data reduction

The *XMM–Newton* X-ray data were originally published in F17 and we refer to that paper for details. We outline the data sets in Table 2, as we do not fit the data that falls on the edges of the chips, for the core, and all the knots. The data reduction was performed using the standard reduction procedures with version 17 of the Science Analysis System (SAS)[5] with Current Calibration Files (CCF) release 358. To produce an X-ray image, we aligned and stacked the MOS1, MOS2, and PN event files from all data sets using the task `evselect` to choose the spectral windows and combined all the epochs and instruments with the FTOOLS task XSELECT. We extracted the X-ray surface brightness profiles of the knots and show updated knot centroid positions in Table 4. We find that the positions differ from those in F17 by 2–7 arcsec, which can possibly be explained by blending of several sources in a crowded field. To have commensurate source extraction regions with F17, we used a source extraction radius of 25 arcsec around the nucleus and removed the background from a region of the same size from a nearby area void of sources and on the same chip. For the individual knots, we employed the same strategy but with a source region radius of 21 arcsec. We checked for pile-up with `epatplot` but found no significant contribution to the spectra over any epoch, chip or source. We corrected the X-ray data for Galactic absorption in the direction of NGC 6217 of 3.90×10^{20} cm^{-2} (Kalberla et al. 2005). As other optical data are available at better than the 4 arcsec angular resolution of the optical monitor (OM), we did not reduce the OM data for these *XMM* observations (see Section 2.3). Due to low count rates on this galaxy, we did not analyse the RGS data.

2.3 Ancillary data

As NGC 6217 is part of the Palomar sample (Filippenko & Sargent 1985; Ho et al. 1995, 1997a,b,c; Ho et al. 1997d,e, 2003, 2009), there exists a large amount of ancillary data in optical and IR surveys. With the intention of fitting the SEDs of all sources coincident with the galaxy nuclear and X-ray jet knot emission, we retrieved data from several missions from IR to optical: *Spitzer*, *Wide-field Infrared Survey Explorer* (*WISE*), Sloan Digital Sky Survey (SDSS), and *Hubble Space Telescope* (*HST*).

There are two observations of NGC 6217 in the *Spitzer* Heritage Archive[6] (AORKEY 30924544, 31025408, PI: K. Sheth). These data were observed at 3.6 and 4.5μm on 2009 October 27 and November 27. We downloaded the already reduced data from the S4G Survey (Sheth et al. 2010) on the NASA Extragalactic Database (NED) website.[7] We then used the software SEXTRACTOR[8] to extract all sources in the 3.6 and 4.5 μm images above a 3σ threshold. We also downloaded the archival *WISE* data from the Infrared Science Archive (IRSA[9]) in the four bands (3.4, 4.6, 12, and 22 μm, Wright et al. 2010) to help give better constraints on the SED fits for the core and knots at different wavelengths. We downloaded SDSS archival data from the DR12 Science Archive Server[10] in all the Johnson *ugriz* filters. We also obtained high-resolution *HST* images of NGC 6217 from the public Hubble Legacy Archive (HLA[11]). We downloaded the *HST*/ACS F814W, F625W, and F435W images (PI: Siranni) taken on the 2009 June 13 and 2009 July 8 to create a three-colour image for reference with regards to the other ancillary data. This colour image is shown with the overlaid contours of the ancillary data and radio images inset in Fig. 2. A Hα-line image (see Fig. 5) was obtained with the *HST*/ACS, through its F658N filter, and reduced as part of the preparatory work for the paper of Comerón et al. (2010). For continuum subtraction an ACS F814W broad-band image was used, following procedures in Knapen et al. (2004), Sánchez-Gallego et al. (2012), and Dullo, Martínez-Lombilla & Knapen (2016).

3 DATA ANALYSIS

Fig. 2 shows all of the ancillary data overlaid on the three colour *HST* image (see the figure caption for an explanation of the contours and sources in different bands). Three X-ray sources appear to spatially align at a PA of $\sim 225°$ from the X-ray source at the centre of NGC 6217. While knots 1 and 2 show more compact X-ray emission, knot 3 reveals two separate components which makes the identification of multiband associations more challenging.

We searched for possible radio (e-MERLIN and VLA) and infrared (IR, *Spitzer*) identification of the knots within the X-ray extraction regions (yellow dashed circles in Fig. 2). The putative X-ray jet shows no evident radio components from the VLA A-Array and e-MERLIN images. However we do detect a single compact source at $16^{h}32^{m}16.99^{s}, +78°10'45.82''$, between X-ray knots 1 and 2, specifically ~ 34 arcsec from knot 1 and ~ 25 arcsec from knot 2. Considering 3σ-significance *Spitzer* 3.6 and/or a 4.5 μm sources, we detected one or two IR associations for each knot within the 21 arcsec X-ray extraction regions. For knots 1 and 2, we only consider

[6]http://sha.ipac.caltech.edu/applications/Spitzer/SHA/
[7]https://ned.ipac.caltech.edu/
[8]https://www.astromatic.net/software/sextractor
[9]http://irsa.ipac.caltech.edu/frontpage/
[10]https://dr12.sdss.org/fields
[11]http://hla.stsci.edu

[5]https://www.cosmos.esa.int/web/xmm-newton/what-is-sas

Table 2. *XMM–Newton* data sets on NGC 6217 from the High Energy Astrophysics Science Archival Research Centre (HEASARC) archive relevant to this paper. The observation ID, observation date, instruments available in each observation, exposure time, and P.I. of each observation.

Obs. ID	Obs. date dd-mm-yyyy	Exposure ks	Core	Knot 1	Knot 2	Knot 3
				Available instruments		
0061940301	20-09-2001	6.1	MOS2[a, b]	MOS1+2[a]	MOS1+2[a]	MOS1+2[a]
0061940901	11-04-2002	9.7	MOS1+2/PN	MOS1+2/PN	MOS1+2[c]	MOS1+2[c]
0400920101	15-02-2007	40.4	MOS1+2/PN	MOS1+2[c]	MOS1+2/PN	MOS1+2/PN
0400920201	17-02-2007	38.9	MOS1+2/PN	MOS1+2[c]	MOS1+2/PN	MOS1+2[c]

Notes. [a]The PN was turned off for this observation. [b]The source fell on the edge of the chip for MOS1. [c]The source fell on the edge of the chip for PN. We refer to the data observed on 2007 February 15 as 2007a, and those observed on the 2007 February 17 as 2007b throughout the rest of this work.

the nearest IR source (<5 arcsec) to the centroid of the X-ray knot as possible identification. For knot 3, one *Spitzer* source lies on one of two distinct components of the X-ray knot (with a separation larger than *XMM–Newton* resolution, see details in Section 3.2). This IR identification is much weaker than the other two X-ray knots.

We also show other sources of radio emission in the inset boxes in Fig. 2, hereafter called secondary sources, with the combined e-MERLIN and VLA data. Inset panel A shows the nuclear region, inset panel B shows a small source south-east of the nucleus on the spiral arm of NGC 6217, inset panel C shows a region of radio emission south of the core and in the bulge of the galaxy, and panel D shows the source along the same PA as the putative X-ray jet mentioned previously, hereafter known as component R for SED fitting purposes (see Section 3.2).

3.1 The new e-MERLIN and VLA data

3.1.1 Radio morphology of the nucleus

The upper left panel of Fig. 3 shows the 10×10 arcsec^2 nuclear region of NGC 6217 for the combined 1.51 GHz e-MERLIN and VLA A-Array data, hereafter referred to as the 'combined' data, with 'Briggs' weighting to show both the diffuse emission provided by the VLA and the compact core regions that e-MERLIN is sensitive to. The combined image shows a two-sided radio structure (PA $\sim 135°$) akin to a 'peanut', with no apparent core at the centre of this structure. Resolving structures such as this is only possible with the e-MERLIN interferometer with its unique combination of subarcsecond and sub-mJy imaging.

The south-eastern lobe-like structure in the combined image is clearly brighter than the north-western one, with an integrated flux density of 18.74 ± 0.24 mJy compared to 11.60 ± 0.22 mJy. There is a hot-spot at $16^h32^m39.39^s$, $+78°11'52.6''$. North of this bright point of emission is a bending arc of radio emission extending ~ 1.5 arcsec north and slightly west. The hotspot in the southern lobe is clearly the brightest source of radio emission in the nuclear region, but it is offset from the nucleus and of similar size to the beam ($0''.20 \times 0''.14$ mas, deconvolved from the beam). It has an integrated flux density of 1.16 ± 0.12 mJy and peak flux density of 0.451 ± 0.034 mJy beam^{-1}. Therefore, it makes up only ~ 5 per cent of the total flux density of this region when compared with the VLA. The north-western region of emission appears clumpy and not well defined by any one structure.

3.1.2 Radio morphologies of the secondary sources

The combined e-MERLIN/VLA images show three radio sources in the environs of NGC 6217, which we discuss here. First, we

see radio emission in the VLA-only and combined images at $16^h32^m38.30^s$, $+78°11'42.9''$ in the spiral arms, seen in inset panel B of Fig. 2 and the top right panel in Fig. 3. It has a slightly resolved two-lobed structure. The VLA-only data show a mostly unresolved source, with flux densities of 0.317 ± 0.041 mJy beam^{-1} (peak) and 0.597 ± 0.114 mJy (integrated). This source has a 3σ *Spitzer* association.

The second source (inset panel C in Fig. 2 and the bottom left panel in Fig. 3) we observe is in projection within the main galactic bulge, only ~ 0.5 arcmin south of the nucleus ($16^h32^m44.73^s$, $+78°11'21.4''$). It appears as a compact source in the VLA-only and combined images, with a possible small extension east, although given the beam size and resolution, it is consistent with being an unresolved source. It also has low VLA flux densities of 0.556 ± 0.044 mJy beam^{-1} (peak) and 0.501 ± 0.074 mJy (integrated).

Interestingly, we find a prominent unresolved source of radio emission at $16^h32^m16.99^s$, $+78°10'45.82''$, along the same P.A. as the putative X-ray jet between knots 1 and 2 of the X-ray emission (see panel D of Fig. 2 and bottom right panel in Fig. 3). The VLA integrated flux density of this source is 1.34 ± 0.16 mJy, which compares to 0.974 ± 0.036 mJy with e-MERLIN. This source was not detected above the 3σ threshold by the SEXTRACTOR procedure, but a weak *Spitzer* source is clearly visible in the image (see Section 3.2).

3.1.3 Radio properties and spectra

The nuclear region appears resolved in the combined data, hence it is possible that we may have lost some flux due to resolving out the diffuse emission that e-MERLIN is not sensitive to. Table 3 shows the flux densities for the core and all of the other radio sources found in the e-MERLIN-only and VLA-only data. We additionally compare the nuclear region to the NVSS values of NGC 6217 to fully consider any diffuse emission in the galaxy. From the NVSS and VLA data, we conclude that we lost ~ 50 per cent of the total emission moving to the longer baseline array. We find a similar drop when comparing the VLA to the e-MERLIN data. Hence, there is diffuse emission that e-MERLIN alone cannot account for in this nuclear region.

As for the three discrete sources of radio emission seen in the VLA images other than the nuclear region, the two sources in panels B and C in Fig. 2 seem to significantly resolve out flux when the e-MERLIN-only (or combined) data is compared to the VLA-only data. For these two sources, e-MERLIN only captures ~ 40 per cent of the total flux for these regions seen in the VLA-A array data. Hence, the diffuse elongations seen by the combined
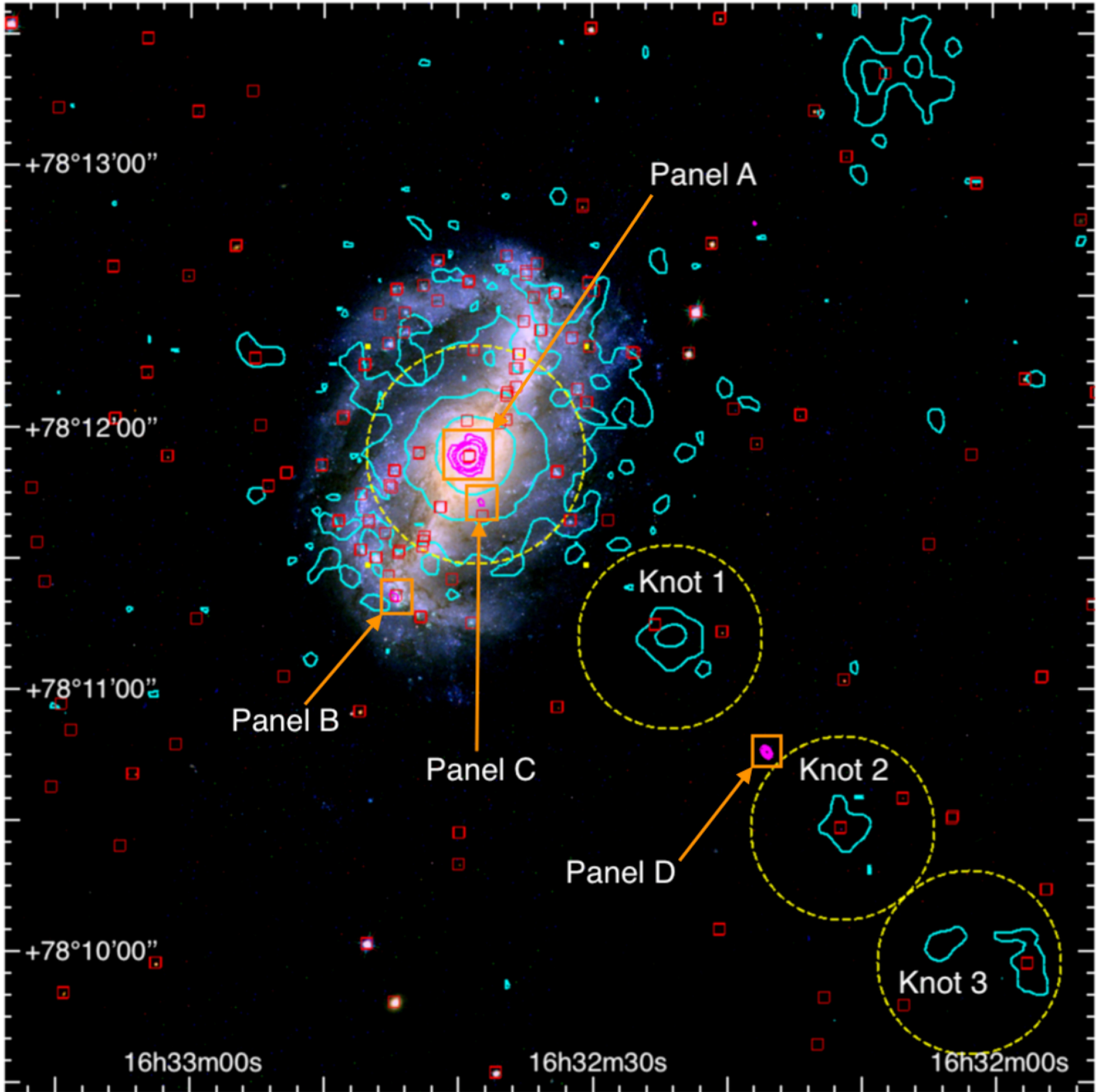
Figure 2. Multiwavelength image of NGC 6217 and the putative 160 kpc X-ray jet from F17, including insets of the nuclear region and three other sources detected with the combined VLA A-array and e-MERLIN data. The background image utilizes *HST* F814W (red), F625W (green), and F435W (blue) images to create a three-colour image of NGC 6217. All three filters are weighted evenly on a linear scale. The cyan colours represent the 7, 12, and 30 count levels of the 0.3–2.0 keV *XMM–Newton* image, was smoothed with a Gaussian filter of radius 2 arcsec. The yellow dashed circles correspond to the *XMM–Newton* data spectral extraction regions for the nucleus, and all the X-ray knots from the updated values in Table 4, with radius the same from F17 and in this paper: 25 arcsec for the nucleus and 21 arcsec for each of the knots. The magenta contours show the VLA A-Array data at 0.25, 0.5, 1.0, and 5.0 mJy beam^{-1}. The red squares denote 3σ detections of sources with the archival 3.6 and 4.5 μm *Spitzer* data. The inset panels are described in Fig. 3 and indicate the 'secondary sources' described in Section 3.1.2. Panel A is the nuclear region of NGC 6217, panel B corresponds to a compact region in the spiral arm of NGC 6217 south-east of the core, panel C is for a small region of radio emission in the galaxy bulge slightly south of the core, and panel D describes a discrete radio source between the X-ray knots 1 and 2, south-west of the core. This figure corresponds to a scale of 4 arcmin × 4 arcmin (25 kpc × 25 kpc). Note the size of the inset squares overlaid on the *HST* image are not to scale. In this figure, north is up and east is left.
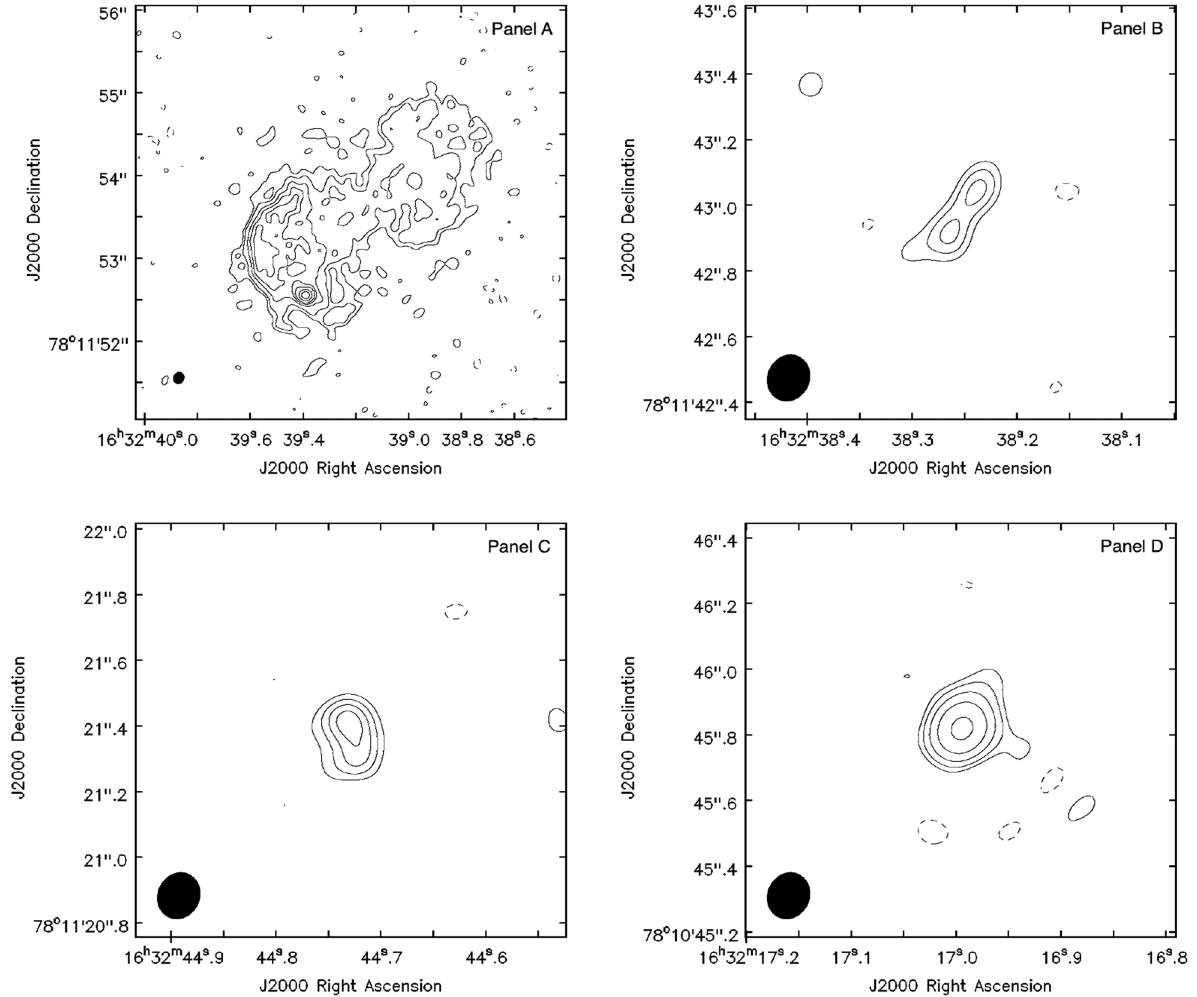
Figure 3. Combined e-MERLIN/VLA A-Array, Briggs-weighted contour images of the sources detected with the VLA. The letters in the top right of each panel correspond to the panels in Fig. 2. The top left is the central 5 arcsec × 5 arcsec, corresponding to 485 × 485 pc, nuclear region in NGC 6217, as previously shown in panel A of Fig. 2. The combined beam (0.14 arcsec × 0.12 arcsec) is shown in the bottom left hand corner as a filled black circle. The contour scale is $-20, 30, 50, 100, 150, 200, 300, 400$, and 500×10^{-6} Jy beam^{-1}. The top right image is the radio source south-east of the nuclear core of NGC 6217, showing a region 1.2 arcsec × 1.2 arcsec, corresponding to 116 × 116 pc, shown previously in panel B of Fig. 2. The beam is 0.14 arcsec × 0.12 arcsec and the contour scale is $-20, 30, 40$, and 50×10^{-6} Jy beam^{-1}. The bottom left image is the radio source directly south of the nuclear core of NGC 6217, shown in panel C of Fig. 2. The beam (0.14 arcsec × 0.12 arcsec) and the contour scale is $-20, 30, 40, 50$, and 60×10^{-6} Jy beam^{-1}. The bottom right image is the radio source south-east of the nuclear core of NGC 6217 and in between X-ray knots 1 and 2, shown in panel D of Fig. 2. The contour scale is $-50, 50, 100, 200, 400$, and 800×10^{-6} Jy beam^{-1} and the beam size is 0.14 arcsec × 0.12 arcsec. In all contour plots, north is up and east is to the left.

e-MERLIN/VLA data may in fact be real for these sources. For the third source in panel D in Fig. 2, e-MERLIN data reproduces over 80 per cent of the total flux density of this source when compared to the VLA data, indicating it is likely a very compact source.

We checked for any variability in the core between the Vila et al. (1990) observations and our new VLA-A array data. The flux densities of our new VLA A-array data and of Vila et al. (1990) agree within errors, indicating that there has likely been no significant change over the period of nearly 30 yr.

Due to the low signal for the nuclear region, it was not possible to make an in-band spectral index image from the 1.51 GHz e-MERLIN observations. However, using the VLA data at 1.51 GHz, we were able to get a crude in-band spectral index using CASA and by setting nterms = 2. We estimate a flat spectral index of -0.2 ($S_\nu \sim \nu^\alpha$), although the uncertainties in this value are likely of order $\pm$ 0.5, as NGC 6217 is not bright enough in the VLA data to properly constrain α. We note that Vila et al. (1990) estimate a compact nuclear spectral index of -1.0 based on archival VLA data at 20 and 6 cm, albeit with a larger beam size.

3.2 Spectral energy distributions

We carried out multiband source identification of the X-ray knots and the VLA-detected radio source, using SDSS *ugriz* bands, the three *HST* ACS bands (F435W, F625W, and F814W), *Spitzer* 3.6 and 4.5 μm data and the four *WISE* bands. We performed aperture photometry on an area which includes the full width at half-maximum of the PSF for each instrument, properly centred on the position of the detected *Spitzer* sources, isolating the genuine emission of the associations and subtracting the background emission. The extracted magnitudes of the detected sources are consistent with the values reported in the IRSA catalogue within the uncertainties. For the sources not detected, we derived 3σ upper limits on the multiband association. The optical–IR magnitudes for our sources are presented in Table 4.

Table 3. Radio flux densities of the core region (panel A in Fig. 2) and all three secondary sources in the inset panels of Fig. 2. All values were obtained from Briggs weighted data, and were made using the CASA 2D fitter where possible, whereas the e-MERLIN integrated flux densities for the core and the individual lobes were obtained using TVSTAT in AIPS due to their being extended in nature. The peak flux density of the core region in the e-MERLIN data was not estimated as it is a resolved source and no radio core is observed between the two e-MERLIN radio lobes. The integrated flux for the entire nuclear region was extrapolated from all of the emission from both the lobes, as the lobes are resolved at e-MERLIN and e-MERLIN/VLA baselines. The e-MERLIN data did not detect the sources in panels B and C alone, hence they have no flux values given, but must be less than three times the noise in the image (0.02 mJy). The columns are presented as follows: (1) is the radio source, (2) is the radio array used, (3) is the integrated flux density from the whole source in the given array, and (4) is the peak flux density from the source.

Radio source (1)	Radio array (2)	Int. flux (mJy) (3)	Peak flux (mJy beam^{-1}) (4)
Total	NVSS	80.3 ± 2.4	57.8 ± 1.1
Northern lobe	VLA e-MERLIN	– 11.60 ± 0.22	– 0.146 ± 0.003
Southern lobe	VLA e-MERLIN	– 18.74 ± 0.24	– 0.205 ± 0.003
Southern hotspot	VLA e-MERLIN	– 1.16 ± 0.12	– 0.451 ± 0.034
Nuclear structure	VLA e-MERLIN	40.4 ± 3.2 29.84 ± 0.16	7.28 ± 0.50 –
Source in panel B	VLA e-MERLIN	0.597 ± 0.114 –	0.317 ± 0.041 –
Source in panel C	VLA e-MERLIN	0.501 ± 0.074 –	0.556 ± 0.044 –
Source in panel D	VLA e-MERLIN	1.34 ± 0.16 0.974 ± 0.036	1.297 ± 0.088 0.955 ± 0.020

We fit the SEDs with the 2SPD code developed by Baldi et al. (2013, 2014). This code allows for the inclusion of two different stellar populations, typically one younger and one older (YSP and OSP, respectively) which correspond to different starburst ages, a dust component with a single (or two) temperature black-body emission(s), AGN spectrum with emission lines. The code searches for the best match between the sum of the different models and the photometric points minimizing the appropriate χ^2 function (see Baldi et al. 2013 for details). The main parameters which 2SPD returns are the photometric redshift and the bolometric luminosity of the source. To estimate the uncertainties on the photo-z and mass derivations, we measure the 99 per cent confidence solutions for these quantities.

The synthetic stellar templates used to model the observed SEDs are from Bruzual & Charlot (2011), with single stellar populations with ages ranging from 1 Myr to 12.5 Gyr. We adopt a dust-screen model for the extinction normalized with the free parameter A_V, and the (Calzetti et al. 2000) extinction law. The emission lines are taken from the AGN atlas covering the ultraviolet to near-IR spectral range from Seyfert or Qusai-Stellar Object (QSO) templates[12] (Francis et al. 1991).

---

[12] http://www.stsci.edu/hst/observatory/crds/cdbs_agn.html

We run the 2SPD fitting code for different sources: X-ray knot 1 associated with *Spitzer* source A, X-ray knot 2 associated with *Spitzer* source B, X-ray knot 3 associated with *Spitzer* source C, and then the VLA radio component with *Spitzer* source R. All of the extracted *HST*, *WISE*, and SDSS sources for all the X-ray knots are detected above 5σ detection significance. For the radio knot, the associated *Spitzer* source has a 2.7σ detection in IRAC1 and 3σ detection for IRAC2. The results from the SED-fitting procedure are found in Table 4. We did not perform SED fitting for the radio sources in panels B and C in Fig. 2 as the multiband contamination from the host galaxy NGC 6217 is significant, preventing an accurate extraction of the genuine emission from those sources.

X-ray knot 1 has two *Spitzer* components within the X-ray spectral extraction region, however we only perform an SED fit for the source (A) at $16^h32^m25.32^s$, $+78°11'15.1''$, which is consistent with the the X-ray knot centroid within the position errors. It is detected only in IRAC bands 1 and 2 (3.5 and 4.5 μm), and *WISE* 1 and 2 bands (3.4 and 4.6 μm). In addition, we detected two *HST* sources 1.2 and 2.5 arcsec away from this *Spitzer* source, but they are not detected in the SDSS. As it is not certain whether and which of the two *HST* sources are genuinely related to the *Spitzer* source, we do not include them in the SED fit. Using the only detections from *Spitzer* and *WISE* W1/W2 bands, *Spitzer* source A has an SED that is consistent with an obscured 6 Gyr old stellar population. The photometric redshift derived is $0.48^{+0.25}_{-0.12}$ and its bolometric luminosity is 7.9×10^{43} erg s^{-1}. The paucity of accurate data points in the SED of this source makes the physical parameters derived from the fit for this source doubtful. Therefore, the uncertainties on the the redshift and bolometric luminosity are likely much larger than that quoted here.

X-ray knot 2 also has two *Spitzer* associations falling in the X-ray extraction region but the closest to the X-ray knot matches with the *Spitzer* position (separation <0.3 arcsec) and is named as *Spitzer* source B ($16^h32^m11.49^s$, $+78°10'28.4''$). It is detected in all the 14 available photometric bands. Its SED shows a rising blue part, flat IR spectrum, and interestingly the g- and z-band associations are significantly brighter than the other adjacent SDSS bands by ∼1.5 magnitudes. The only physical interpretation of those broad-band peaks is the contribution from emission lines in the bandwidths of g and z bands. The best-fitting model of the SED includes a Seyfert/QSO-like spectrum, which is able to reproduce simultaneously the blue spectral rising and emission lines, Mg II and an Hβ, which contribute to ∼70 and ∼66 per cent of the total flux in the g and z bands, respectively. The wavelength of the emission lines within the SDSS bands constrains the photo-z at $0.70^{+0.03}_{-0.02}$. The near- and mid-IR data are modelled by a 3-Gyr old stellar population and two-temperature black bodies. The bolometric luminosity is 8.3×10^{43} erg s^{-1}.

As mentioned previously, the shape of X-ray knot 3 is convoluted as it is made up of two distinct X-ray components which makes the centroid difficult to determine. The western part of this knot ($16^h31^m57.66^s$, $+78°09'57.0''$) aligns well with *Spitzer* source C, which is detected in all bands, except the last two *WISE* bands. The blue spectral rising has been fitted with a YSO of 0.03 Gyr and the optical and near-IR region with an OSP of 4 Gyr. The contribution from an AGN is not needed to fit the optical–IR data points. As the blue spectral curvature is the only feature to constrain the photometric redshift, this results in a mediocre photo-z determination, corresponding to $0.46^{+0.19}_{-0.06}$. The bolometric luminosity is 9.3×10^{43} erg s^{-1}. The tentative identification of the X-ray knot with the *Spitzer* source C must be taken as a reasonable

Table 4. The multiband magnitudes and fluxes of the sources found coincident with the three X-ray knots and the radio knot (panel D of Fig. 2). The positions of the X-ray knots and *Spitzer* sources are given, as well as the difference in position, Δ, which was calculated from the difference of the *Spitzer* source position and our X-ray knot centroids. The SDSS, *HST*, and *WISE* values are given in AB magnitudes and the IRAC data are given in mJy. The photometric redshift and corresponding bolometric luminosities are given for all of the sources, ascertained from the 2SPD fitting code of Baldi et al. (2013) and Baldi et al. (2014). The photon index, Γ, and the corresponding fluxes and luminosities of each of the X-ray knots is also given, found from the X-ray spectral fitting process in Section 3.3. We show the X-ray luminosities given the distance to NGC 6217 (see Introduction) and the photometric redshifts ascertained from the SED fits. The errors on the X-ray luminosities include only the uncertainties in the fluxes, and not the distance.

X-ray knot	1	2	3	Radio
RA	$16^h32^m24.21^s$	$16^h32^m24.21^s$	$16^h32^m01.93^s$	–
DEC	$+78°11'53.8''$	$+78°11'12.0''$	$+78°09'57.5''$	–
Associated source	A	B	C	R
RA	$16^h32^m25.32^s$	$16^h32^m11.49^s$	$16^h31^m57.66^s$	$16^h32^m16.99^s$
DEC	$+78°11'15.1''$	$+78°10'28.4''$	$+78°09'57.0''$	$+78°10'45.8''$
Δ	$4.62''$	$0.48''$	$13.15''$	–
SDSS u	<22.15	22.27 ± 0.37	21.93 ± 0.24	<22.20
SDSS g	<22.20	20.43 ± 0.03	22.00 ± 0.10	<22.30
SDSS r	<22.40	21.91 ± 0.14	21.65 ± 0.11	<22.20
SDSS i	<21.40	21.71 ± 0.17	21.32 ± 0.11	<21.20
SDSS z	<21.45	20.55 ± 0.25	21.35 ± 0.42	<21.60
HST F425W	–	21.32 ± 0.15	22.10 ± 0.13	< 22.71
HST F625W	–	21.19 ± 0.14	21.55 ± 0.15	< 22.21
HST F814W	–	21.58 ± 0.14	–	<22.42
WISE W1	16.02 ± 0.30	17.42 ± 0.09	17.30 ± 0.07	18.03 ± 0.18
WISE W2	16.01 ± 0.20	16.18 ± 0.10	17.13 ± 0.22	17.73 ± 0.48
WISE W3	<12.28	12.50 ± 0.27	<12.96	<13.20
WISE W4	<8.19	9.02 ± 0.29	<9.40	<9.65
IRAC 1	55.10 ± 8.72	39.34 ± 4.91	29.35 ± 5.35	19.00 ± 6.80
IRAC 2	58.45 ± 7.25	51.57 ± 4.23	31.11 ± 4.40	22.56 ± 7.34
z_{phot}	$0.48^{+0.25}_{-0.12}$	$0.70^{+0.03}_{-0.02}$	$0.46^{+0.19}_{-0.06}$	$0.19^{+0.25}_{-0.12}$
L_{bol} ($\times 10^{43}$ erg s^{-1})	$7.9^{+13.8}_{-3.9}$	$8.3^{+0.9}_{-0.7}$	$9.3^{+12}_{-2.7}$	$0.46^{+2.69}_{-0.40}$
Photon index, Γ	$1.59^{+0.27}_{-0.25}$	$1.38^{+0.45}_{-0.37}$	$1.54^{+0.54}_{-0.46}$	–
Total flux 0.3–10 keV ($\times 10^{-14}$ erg s^{-1} cm^{-2})	$6.92^{+2.20}_{-1.67}$	$4.37^{+3.58}_{-2.46}$	$4.27^{+3.32}_{-2.08}$	<0.3
Unabs. flux 0.3–10 keV ($\times 10^{-14}$ erg s^{-1} cm^{-2})	$8.13^{+2.34}_{-1.96}$	$4.79^{+3.73}_{-2.65}$	$4.90^{+3.42}_{-2.33}$	<0.3
$L_{X\text{-ray, Unabs}}$ at NGC 6217 ($\times 10^{39}$ erg s^{-1})	$3.93^{+1.13}_{-0.95}$	$2.32^{+1.80}_{-1.29}$	$2.37^{+1.65}_{-1.13}$	<0.13
$L_{X\text{-ray, Unabs}}$ at photo-z ($\times 10^{43}$ erg s^{-1})	$7.58^{+2.18}_{-1.83}$	$17.33^{+13.51}_{-9.58}$	$4.13^{+2.88}_{-1.96}$	<0.13

attempt to infer the multiband properties of this X-ray knot without giving any confidence in its correctness.

We also performed an SED fit for the radio component in the inset panel D in Fig. 3, bottom right panel, detected with the VLA and coincident with *Spitzer* source R. Its radio emission is unresolved and lies along the putative 'X-ray jet' in NGC 6217 between knots 1 and 2. Its association with one of the two X-ray knots seems to be unlikely due to its large relative distance (>25 arcsec). This source is detected at near-IR wavelengths (two IRAC and two *WISE* bands). The resulting SED fitting returned an obscured 4 Gyr old stellar population with a photometric redshift of $0.19^{+0.25}_{-0.12}$ and a bolometric luminosity of 4.6×10^{42} erg s^{-1}. The small number of photometric data points reflects on a poor accuracy of its photo-z determination. Therefore, the values inferred for this component must be considered with caution and are meant to provide a possible interpretation of this radio component.

To improve our understanding of the nature of the X-ray knots and the radio component R, we included the radio and X-ray datapoints in the SEDs and we plotted with AGN templates taken from literature (see Fig. 4): radio-quiet type-I and type-II Seyfert/QSO from Ruiz et al. (2010) and a radio-loud low-luminosity AGN from

Chiaberge et al. (2003). The X-ray-radio SED of X-ray knot 1 (*Spitzer* A) is consistent with the SED of a type-II Seyfert galaxy (NGC 4507, $N_H = 4 \times 10^{23}$ cm^{-2}), while the SEDs of other two X-ray knots (*Spitzer* B and C) can be reproduced by a type-I quasar (bolometric luminosity of 10^{10} solar luminosities, Hopkins, Richards & Hernquist 2007). Not surprisingly, the radio source R has an SED smilar to a local radio galaxy, NGC 6251 (Chiaberge et al. 2003). These SEDs suggest that a background-AGN nature of the X-ray and radio sources is a plausible scenario.

3.3 X-ray data analysis

3.3.1 X-ray spectral fits

We first rebinned the spectra using the grppha command in FTOOLS. As there were more than 200 counts in the core spectrum, it was binned with 15 counts per bin for both 2007 data sets and we used χ^2 statistics. For all the knots in all epochs, and the 2001 and 2002 data for the core region, there were too few counts to fit with χ^2 statistics. Hence, we binned these data with 1 count in each bin and used Cash statistics (Cash 1979) to fit them, which is
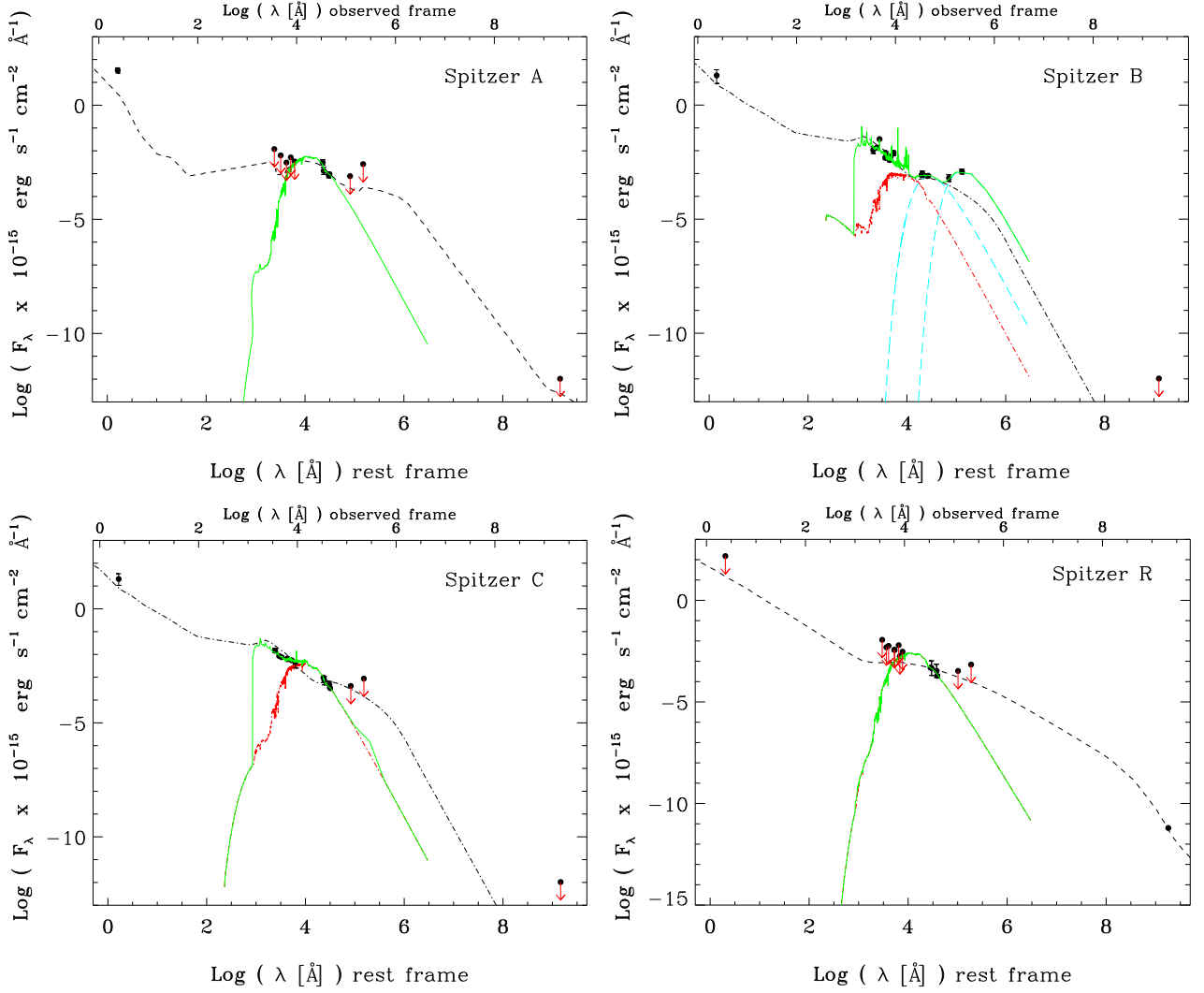
Figure 4. Optical–IR SEDs of the multiband associations of the X-ray knots (Table 2) and the VLA radio component. The first X-ray knot is associated with *Spitzer* source A (upper left panel), X-ray knot 2 with *Spitzer* source B (upper right panel), X-ray knot 3 with *Spitzer* source C (lower left panel), and then the radio component detected with the VLA as *Spitzer* source R (lower right panel). The photometric points are fit with the 2SPD fitting code: the stellar population is the red (dotted–dashed) line, the dust Black-body components are the light-blue (dashed) lines and the total model is the green solid line, which also can include the emission line template. The black dashed lines are the X-ray-radio SEDs of AGN templates taken from Ruiz et al. (2010) and Chiaberge et al. (2003) (see Section 3.2 for details). For all the panels, the wavelengths on the top of the plots correspond to observed wavelengths, while those on the bottom are in the rest frame.

more appropriate in the low-counts regime. The rebinned spectra (see Section 2.2) were loaded into XSPEC version 12.8.2 (Arnaud 1996) and we fitted each spectrum in the energy range 0.3–10.0 keV for each epoch and CCD chip separately to ascertain whether there was any variability in any of the sources across the six years of data. We found no evidence for variability, although we note that there are a low number of counts in some of the observations, especially in the 2001 and 2002 data sets, which makes a conclusion on the variability difficult.

We chose to fit each of the four epochs (2001, 2002, 2007a, and 2007b) separately, fitting the X-ray data for each chip simultaneously due to the different responses of the PN, MOS1, and MOS2 detectors. We used a cross-calibration weighting factor in the spectral fitting process between the PN, MOS1, and MOS2 detectors. We allowed the cross-calibration constant between the instruments to take into account differences in absolute flux calibration and as such all fluxes given are relative to the PN detector. We fitted all the

X-ray knots and the core with the same X-ray spectral models as F17 and compared their results.

3.3.2 Nuclear region spectral fits

F17 found that the best-fitting model (named MEPL) was an absorbed power law with an additional thermal component due to a collisionally ionized plasma. We give the best-fitting parameters of the MEPL model from our X-ray spectral analysis in Table 5 for the 2007 data sets. The X-ray fit parameters (e.g. photon index, see Table 5) ascertained from the two 2007 data sets agree with one another within the uncertainties. The parameters for the 2001 and 2002 data sets also agree with the 2007 epochs within the uncertainties, despite having much lower count rates. Therefore, the nuclear region did not vary over the four epochs. As the data for the 2001 and 2002 epochs did not have enough counts in the MOS detectors to use χ^2 statistics, we only give the values for the

Table 5. Spectral fits of the nuclear region of X-ray emission in NGC 6217 for the 2007a and 2007b epochs. The models are outlined in Section 3.3. Γ refers to the photon index of a power-law fit, with a respective normalization of the photon index 'Photon Index, norm'. kT and norm refer to the temperature and normalization of the thermal component. The reduced χ^2 statistic (χ^2/d.o.f.) is given for the core, where there are sufficient counts to model the data. The total flux was calculated using the XSPEC flux command, and is given for all models and data sets in the 0.3–10.0 keV energy range, as well as those corrected for absorption. All fluxes are given in the units of erg cm^{-2} s^{-1}. All errors are to 90 per cent confidence level.

Parameter (1)	2007a (2)	2007b (3)
Constant (MOS 1)	$1.03^{+0.09}_{-0.08}$	$0.98^{+0.08}_{-0.07}$
Constant (MOS 2)	$1.02^{+0.09}_{-0.08}$	$1.04^{+0.08}_{-0.08}$
Photon index, Γ	$2.37^{+0.17}_{-0.18}$	$2.29^{+0.15}_{-0.14}$
Photon index, norm. ($\times 10^{-5}$)	$2.36^{+0.35}_{-0.34}$	$2.47^{+0.32}_{-0.31}$
kT, keV	$0.78^{+0.03}_{-0.02}$	$0.74^{+0.03}_{-0.02}$
Norm ($\times 10^{-5}$)	$5.46^{+0.43}_{-0.42}$	$5.32^{+0.37}_{-0.36}$
χ^2/d.o.f.	98/87	121/100
Reduced χ^2	1.12	1.21
Total flux 0.3–10.0 keV ($\times 10^{-13}$)	$2.18^{+0.13}_{-0.09}$	$2.20^{+0.12}_{-0.09}$
Unabs. flux 0.3–10.0 keV ($\times 10^{-13}$)	$2.55^{+0.14}_{-0.11}$	$2.62^{+0.14}_{-0.13}$
Total lum. 0.3–10.0 keV ($\times 10^{40}$)	$1.05^{+0.07}_{-0.04}$	$1.06^{+0.06}_{-0.04}$
Unabs. lum. 0.3–10.0 keV ($\times 10^{40}$)	$1.23^{+0.09}_{-0.06}$	$1.27^{+0.07}_{-0.06}$

two 2007 data sets fit separately in Table 5. We note that the photon index obtained in our analysis is slightly lower than that obtained in F17, likely due to the wider band 0.3–10.0 keV band used for fitting.

3.3.3 Spectral fits for the X-ray knots

We employed the same simultaneous fitting method outlined in Section 3.3 for all of the knots separately. We fit an absorbed power law (as in F17) for the knots and we found that the parameters (photon index, Γ and power-law normalization) agreed with one another between observations, for each knot separately. We used the redshifts obtained from Section 3.2 as well as the redshift for NGC 6217 ($z = 0.0045$ and $d = 20.1$ Mpc, Cabrera-Lavers & Garzón 2004) for the spectral analysis of all the knots, but found no difference in the fit parameters or validity of the fits.

Although our spectral fits agree with F17 to within the uncertainties, the errors on the fit parameters are large, especially in the 2001/2002 data sets, mainly due to the low number of counts. Overall, in the full spectral range fitted (0.3–10 keV), there were 291 ± 28 counts in knot 1, 145 ± 12 counts for knot 2, and 181 ± 35 counts for knot 3. Above 3 keV, there are 93 ± 10 counts in knot 1, 37 ± 9 counts in knot 2, and 28 ± 6 counts for knot 3. In addition, we note that for knots 1, 2, and 3, we find photon index values for the 2007 data ($1.59^{+0.27}_{-0.25}$, $1.38^{+0.45}_{-0.37}$, and $1.54^{+0.54}_{-0.46}$, respectively) agree within the uncertainties to the values found in F17, but our absolute values are slightly smaller than those in F17 (1.74, 1.71, and 1.70 for each knot respectively). We attribute this discrepancy to using a wider spectral energy range in our procedure, although we note that we get similar results when using the same spectral range of F17. However, we do not attempt to combine all of the data into one data set for each knot, nor do we attempt a fit of all epoch data for all knots as the photon statistics for each knot is so

poor that any approach might turn in similar fit results because of the large uncertainties.

If we assume that the sources are all at the same distance as NGC 6217, the unabsorbed X-ray luminosities in the 0.3–10.0 keV energy band for knots 1, 2, and 3 are $3.93^{+1.13}_{-0.95} \times 10^{39}$, $2.32^{+1.80}_{-1.29} \times 10^{39}$, and $2.37^{+1.65}_{-1.13} \times 10^{39}$ erg s^{-1} respectively. However, if we consider the distances found in Section 3.2, we arrive at values of $7.58^{+2.18}_{-1.83} \times 10^{43}$, $1.73^{+1.35}_{-0.96} \times 10^{44}$, and $4.13^{+2.88}_{-1.96} \times 10^{43}$ erg s^{-1} for knots 1–3, respectively.

4 DISCUSSION

4.1 The nuclear region of NGC 6217

As noted previously, the optical classification of the nucleus is debated in the literature (see Introduction) whether its optical spectrum is dominated by an AGN or SF. We investigate two main possibilities: twin-lobed radio emission caused by an LLAGN or a compact star-forming region in the centre of NGC 6217. We also consider whether a combination of both LLAGN activity and SF can explain the observed multiwavelength emission.

4.1.1 An LLAGN origin

As explained in Section 3.1, there are two radio lobe-like structures extending ~ 3 arcsec north-west and south-east of the optical nucleus. Furthermore, the southern lobe-like feature is more prominent than the northern one, with complex structures and a bright hot-spot. No core has been detected in the radio images. Morphologically, the twin-lobed radio structure of NGC 6217 is similar to an expanding radio cocoon, consistent with compact steep spectrum (CSS) or gigahertz-peaked (GPS) sources (Orienti 2016). However, CSS and GPS sources typically show two bright hotspots but we only observe one in NGC 6217.

The radio structures do not unambiguously match with the line emitting region in the Hα *HST* image. However, assuming an astrometric error of 0.3 arcsec of the *HST* image, we note there exists a small faint region of Hα emission, approximately located at the centre of the total radio structure. This optical centre likely corresponds to the centre of the galaxy and the location of the AGN.

By considering the radio and X-ray properties of NGC 6217, we discuss whether an LLAGN is present at the centre of the galaxy. With regard to the X-ray spectra, the photon index ($\Gamma = 2.3$) is a little higher than the range reported in the literature for typical AGN ($\Gamma \sim 1.5$–2.1, Nandra & Pounds 1994; Reeves & Turner 2000; Piconcelli et al. 2005; Page et al. 2005; Ishibashi & Courvoisier 2010), although not completely inconsistent with some of the sources reported in those publications. Furthermore, soft X-rays from the inner jet (e.g. Hardcastle, Croston & Kraft 2007) may increase the photon index. Additional, unresolved, nuclear components like an ultraluminous X-ray sources or X-ray binaries (XRB, e.g. Stobbart, Roberts & Wilms 2006) may also add additional soft photons to the nuclear X-ray spectrum. The low resolution of the X-ray data, which encompasses most of the optical extent of the galaxy, makes it impossible to conclude definitively whether an additional nuclear component is adding to the X-ray spectrum. Regarding the radio emission, similar edge-brightened radio structures have been observed with the e-MERLIN array in nearby galaxies hosting LLAGN (see LeMMINGs, Baldi et al. 2018a). In addition, the orientation of the radio lobe structures along the major axis of the galaxy strengthens the AGN scenario, since

starburst superwinds tend to produce radio bubbles aligned with the minor axis (Ulvestad & Wilson 1984; Baum et al. 1993; Colbert et al. 1996; Kinney et al. 2000; Gallimore et al. 2006; Robitaille et al. 2007; Irwin et al. 2017). Therefore, assuming that the radio structure is powered by the central BH, two possible classes of LLAGN can be considered: LINERs and Seyferts.

LINERs typically show more core-brightened radio morphologies than NGC 6217, but several cases of parsec-scale double-lobed jetted structures associated with LINERs are present in the LeMMINGs survey. The multiband luminosities of the nucleus lead to aN LINER scenario. In fact, the comparison of the [O III] line luminosity, measured from the Palomar survey, 1.78×10^{39} erg s^{-1} with the 2–10 keV unabsorbed nuclear luminosity, set NGC 6217 in a region occupied mostly by LINER-like sources in the X-ray–[O III] diagram (Hardcastle, Evans & Croston 2009; Torresi et al. 2018). Furthermore, our e-MERLIN radio observations yield an upper limit of the 1.51 GHz luminosity of the core of 1.91×10^{35} erg s^{-1}, which when compared to the $L_{core} - L_{[O III]}$ relation of Baldi et al. (2018a, their fig. 6) falls in the region of the LINERs. Another argument in favour of the LINER scenario is the location of this target in the Fundamental Plane of BH activity in the optical band (see Saikia, Körding & Falcke 2015; Saikia, K örding & Dibi 2018) within the region covered by LINERs (Baldi et al. 2018a, their fig. 8). Furthermore, F17 extrapolated the NVSS flux for NGC 6217 to 151 MHz and found it consistent with a LINER based on radio, IR, and X-ray properties (Mingo et al. 2016). In addition, F17 calculated the logarithm of the Eddington ratio for NGC 6217 as −4.09, consistent with a low-level accreting AGN such as LINERs.

Seyfert galaxies typically show large-scale AGN-driven outflows (Colbert et al. 1996), which appear in radio as double-lobed and less diffuse than radio structures of LINERs (Baldi et al. 2018a). Similar morphologies have been observed in the Narrow Line Seyfert 1 galaxy Mrk 783 (Congiu et al. 2017), which has a similar southern edge-brightened lobe and hotspot seen in NGC 6217. There have been a number of other investigations into Seyfert nuclei showing similar pc–kpc 'bubble-like' structures, attributed either to AGN activity, SF or a combination of the two (Wilson & Ulvestad 1983; Elmouttie et al. 1998; Kukula et al. 1999; Hota & Saikia 2006; Kharb et al. 2006, 2010; Nyland et al. 2017; Ramírez-Olivencia et al. 2018).

Another possible scenario is a 'relic' radio source, supported by the lack of a clear core and the diffuse relaxed bubble morphology. A similar conclusion of a turned-off AGN has been drawn for Mrk 783 by Congiu et al. (2017), based on the steep-spectral index of the lobe. To explore this possibility, we calibrated archival Very Long Baseline Array (VLBA) data on NGC 6217 at 8 GHz using the AIPS VLBA pipeline VLBARUN. The VLBA data show no detection of NGC 6217 at the 5-sigma level (rms noise 3×10^{-4} Jy beam^{-1}). These data could either suggest that the core is extremely weak, or the AGN is currently inactive, or that the radio core has an inverted spectral index with a turnover frequency greater than 8 GHz, similar to that seen in NGC 7674 (Kharb, Lal & Merritt 2017).

4.1.2 A star formation origin

Fig. 5 shows a large amount of nuclear Hα emission but not aligned with the radio emission, possibly caused by diffuse SF. In fact, the optical *HST* ACS F814W image of NGC 6217 shows the presence of strong SF in the galaxy and across the spiral arms. In addition, an inner stellar ring with radius $\sim$1.3 arcsec, with a dust spiral roughly at the radius of this inner stellar ring, is present. Certainly, there

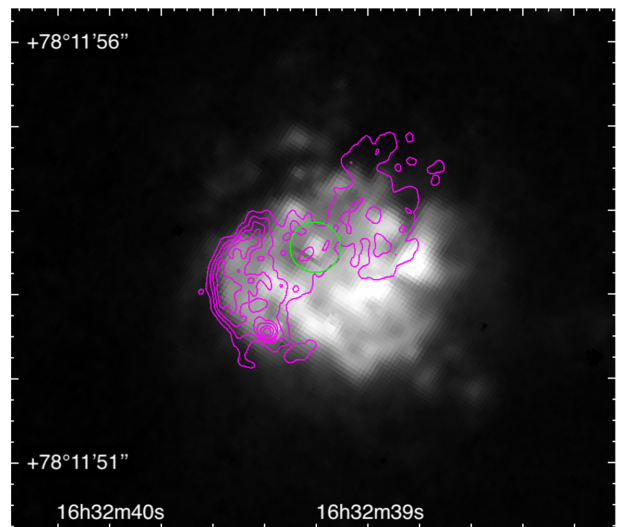**Figure 5.** The *HST* Hα image of the central 7 arcsec $\times$ 7 arcsec, corresponding to 680 $\times$ 680 pc, nuclear region in NGC 6217, overlaid with the radio contours from the combined e-MERLIN/VLA data in magenta. The radio contours are set at 50, 100, 150, 200, 300, 400, and 500 $\times$ 10^{-6} Jy beam^{-1}. The green circle is centred on the hottest pixel in the Hα image and the radius corresponds to the typical *HST* offset of 0.3 arcsec. North is up and east is to the left.

is SF that is contributing to the observed multi-wavelength nuclear properties of NGC 6217. Therefore, all these features may suggest an SF-related origin of the radio structure of NGC 6217 observed with e-MERLIN.

The ratios of emission lines taken from the optical spectrum provided by the Palomar survey (Ho et al. 1997a,b) ([N II], [S II], [O III], and [O I] forbidden lines and the Hα and Hβ lines) are used to diagnose the nature of gas ionization in the so-called BPT diagrams (Baldwin, Phillips & Terlevich 1981; Kewley et al. 2006; Buttiglione et al. 2010). NGC 6217 falls into the region of star-forming galaxies in this diagram (Fig. 6), consistent with Palomar survey classification (Ho et al. 1997b), despite the updated separation between AGN- and SF-dominated area in the BPT diagrams introduced by Kewley et al. (2006). However, it is worth mentioning that the Palomar optical spectra were obtained with a slit of effective aperture 2–4 arcsec in size, which would include most of the SF visible in the *HST* image for our object. Therefore, it is also possible that an LLAGN is still hidden in the very centre, but not contributing significantly to the line emission.

Parsec-scale radio bubbles have been observed in local star-forming galaxies (e.g. see the LeMMINGs survey, Baldi et al. 2018a). These lobed structures can be driven by superwind bubbles inflated by SNe (Pacholczyk & Scott 1976; Heesen et al. 2009). We computed the energy budget of the lobes assuming that they could be driven by a nuclear starburst using a similar process as described in Kharb et al. (2006) for Mrk 6, a local galaxy which a radio structure similar to NGC 6217. This methodology involves computing the time for a lobe to expand to the observed physical size and comparing this to time taken for SNe to explain the observed emission, assuming adiabatic expansion. We calculate the volume of each lobe assuming the lobes are spherical with a radius ($r \sim 0.3$ kpc). The pressure within the interstellar medium is $\sim 10^{10}$ dyne cm^{-2} and the energy required is therefore $4PV \approx 3.2 \times 10^{53}$ erg. Kharb et al. (2006) postulate an average SNe energy of 10^{51} erg, which if applied here requires 3.2×10^2 SNe in this nuclear region.
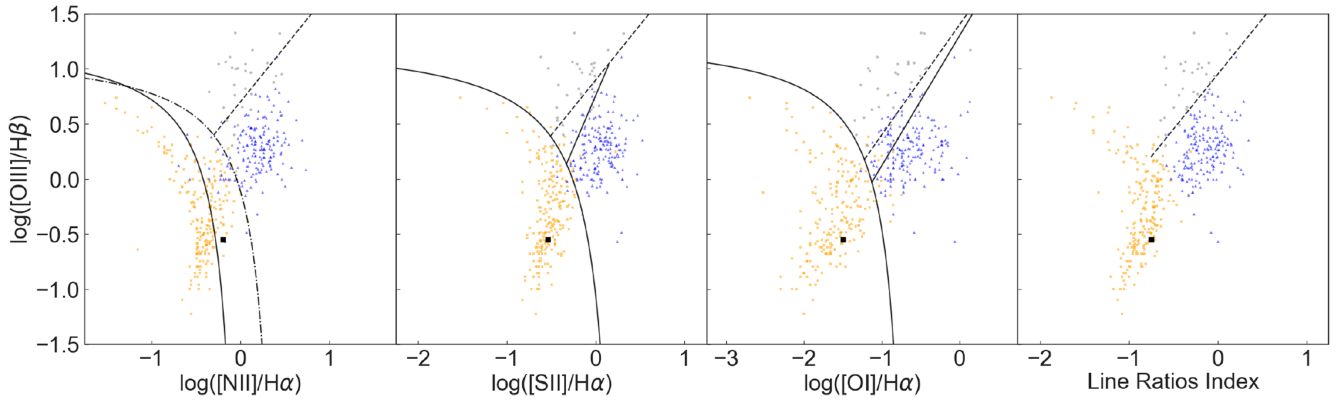
Figure 6. BPT emission-line diagnostic diagrams for NGC 6217. Going from left to right, the panels show the $\log[\text{O III}]/\text{H}\beta$ ratio against (panel 1) $\log[\text{N II}]/\text{H}\alpha$, (2) $\log[\text{S II}]/\text{H}\alpha$, (3) $\log[\text{O I}]/\text{H}\alpha$, and (4) line ratios index. The position of NGC 6217 in the diagrams is shown by the black squares. The black lines are the Kewley et al. (2001) diagnostic lines, the dot-dashed line in the first panel shows the Kewley et al. (2006) maximum starburst line and the dashed lines show the Buttiglione et al. (2010) classification between LINERs and Seyferts. The BPT diagram for the whole Palomar sample (Ho et al. 1997a) is shown in the background, with H II galaxies in orange, LINERs in blue, and Seyferts in grey.

Assuming wind speeds of $10^3 \, \text{km s}^{-1}$, it would take $\sim 3 \times 10^5$ yr to inflate the 'bubble' to its present size, requiring SNe rate of $\sim 1.1 \times 10^{-3} \, \text{yr}^{-1}$. This value for the SNe rate is similar to that calculated for M 82 for a nuclear region of a similar size to that shown here for NGC 6217 (Baldi et al. 2018a). Hence, this calculation energetically shows that the SF scenario for the radio emission of NGC 6217 is plausible.

Another argument in favour of the SF scenario is the low-brightness temperature T_{B} observed in the NGC 6217. T_{B} is a metric that is often used to discriminate compact, star-forming H II regions from AGN as H II regions tend to be limited to $T_{\text{B}} \lesssim 10^5 \text{K}$ (Condon 1992). For objects above this threshold, additional emission from relativistic electrons from the AGN is required to explain the high-brightness temperature. The low T_{B} measured for our target suggests that SF can account for the low-brightness diffuse emission detected in the e-MERLIN image. However, as pointed out by Baldi et al. (2018a), since brightness temperatures depend on the flux densities and the sizes, at e-MERLIN resolution and sensitivity only sources brighter than 5 mJy beam^{-1} can yield brightness temperatures greater than 10^6 K. Therefore, even considering the brightest unresolved component in NGC 6217, which is the southern hotspot with 0.45 mJy, T_{B} is far below the separation threshold between AGN and SF. Therefore, the low T_{B} cannot provide a conclusive answer to the nature of the the faint extended radio emission in NGC 6217.

4.1.3 An LLAGN and SF origin

Due to the large amount of contrary evidence, it is difficult to conclude with certainty whether the observed radio emission is due to SF or an LLAGN. Another possibility for the observed multiband emission, is that both an LLAGN and SF contribute to different observed properties. This interpretation is supported by the large ongoing SF visible in the *HST* images and the radio and X-ray properties, more consistent with a phenomenon of accretion on to a supermassive BH. We conclude that the nuclear region of NGC 6217 probably contains a LINER-type LLAGN, similar to some of the H II galaxies observed in the LeMMINGs 'shallow' sample (Baldi et al. 2018a). However, the contribution from second nuclear component like XRBs cannot be ruled out given the data resolution. Hence, we agree with the conclusions of F17 regarding the combined AGN and

SF origin of the nuclear emission. Higher resolution (e.g. *Chandra*) X-ray data are required to properly understand the nuclear properties of this source.

4.2 The putative X-ray jet of NGC 6217

A detailed analysis of the X-ray data in NGC 6217 is presented by F17, who consider *XMM–Newton* observations. In addition to emission from the galaxy itself, they note three X-ray emission knots in a line along a PA of $\sim 225°$ (Fig. 2), oriented towards the galaxy, with the most distant being ~ 15 kpc from the nucleus. They find no optical associations in the XMM–OM images or the SDSS data for knot 1. For knot 2, F17 find one associated source, at 1.6 arcsec away from the X-ray position in the OM *u* filter and a further source in the SDSS *r* band at 0.9 arcsec away, but conclude that these sources are likely unrelated stars. For knot 3, F17 found an association with an SDSS source 1.2 arcsec away but conclude that it is likely from a passive spiral galaxy.

F17 note that radio emission from the galaxy in low-resolution NVSS images shows a low-brightness 2 arcmin elongation along the line of the three X-ray components. They consider various scenarios to explain the X-ray and radio emission components, including background sources, but eventually favour a jet origin. They do however, note that higher resolution radio observations are required to confirm at least the radio extension as coming from a jet. Here, in the light of such higher resolution radio observations, we question the jet origin of the radio and X-ray emission.

We first consider the radio emission. From our e-MERLIN and VLA observations, we can clearly see emission on the scale of a few arcseconds associated with the galaxy itself. In addition, three very compact (subarcsecond) sources are observed, one of which lies exactly along the putative radio extension shown in the NVSS images but not associated with the X-ray knots. We explore the nature of this radio component in Section 4.3. It is unlikely that a radio jet structure exists in the intermediate scales between the resolution of the VLA in A Array at 1.51 GHz (beam size ~ 1 arcsec) and the NVSS survey (beam size ~ 45 arcsec) as archival VLA data[13] in C configuration and at 1.51 GHz (beam size ~ 16

---

[13]Images obtained from the VLA Imaging Pilot, https://archive.nrao.edu/nvas/

arcsec) show only an unresolved source and no extension in any direction. Moreover, van Driel & Buta ([1991]) show no extension towards the X-ray jet in H I images of NGC 6217 at a resolution of 20 arcsec. Thus, from this new high-resolution data and archival data sets, it is possible to exclude the presence of a large-scale radio jet associated with the X-ray jet in NGC 6217. The lack of radio jet leaves a gap in our knowledge of the aligned X-ray knots and motivates new high-resolutions X-ray observations with *Chandra*. We discuss the scenario where all of the X-ray knots are possibly background sources in the next two sections.

The interpretation of a lack of a radio emitting jet is supported by the global properties of NGC 6217. In fact, there are no examples in the literature of sources similar to our target, i.e. low-luminosity radio-quiet AGN with a small BH mass (2.0×10^6 M$_\odot$), which can launch radio jets that are also visible in the X-rays. This is a restrictive prerogative of powerful radio-loud AGN, which show large kpc-scale collimated jets and massive BH ($>10^8$ M$_\odot$). There are some rare cases of X-ray jets observed without any associated radio jet (see e.g. Simionescu et al. [2016]; Meyer et al. [2017]; Hlavacek-Larrondo et al. [2017]), but we note that these jets are found in very luminous galaxies with powerful AGN also, unlike NGC 6217.

4.2.1 Chance alignment of the X-ray knots

We now consider the likelihood of the X-ray knots appearing to align by chance. First, we ascertain whether the *Spitzer* sources are genuinely related to the X-ray knots. We computed the number of 3σ *Spitzer* detections that are expected in one of the circular 21 arcsec X-ray extraction regions, from the *Spitzer* catalogue (e.g. the red squares in Fig [2]). We found 148 *Spitzer* detections in the 5.2 arcmin × 5.2 arcmin *Spitzer* CCD field-of-view, corresponding to ∼2 sources per 21 arcsec radius spectral extraction region. We find two 3σ detections in the spectral extraction region of knots 1 and 2, and one detection in the spectral extraction region for knot 3, although a second object is very close to said region (see Fig. [2]). Hence, the number of *Spitzer* objects in each extraction region is consistent with the number expected from this simple analysis.

Further to the analysis of the cospatiality between *Spitzer* sources and the X-ray knots, we calculated the likelihood of the three X-ray knots forming a line from the centre of NGC 6217 by chance. To perform this statistical analysis, we used the integral source counts for *XMM–Newton* (Ranalli et al. [2013]). First, we calculated the number of sources we would expect in a given radius from the nucleus to knot 1. We then found the number of sources in the radius from knots 1 to 2 and multiplied this value by the angle subtended by knot 2 on knot 1. We performed this step again, but for knots 2 and 3. The product of these three values gives us a small probability of chance alignment of 1.37×10^{-4}. However, we also consider the sources that both the NVSS and *XMM–Newton* have observed to estimate the likelihood of seeing such an alignment present in NGC 6217. As an example, we use the NGC catalogue, which has 7840 galaxies present. Of these, 7074 sources have been observed by the NVSS. Of these 7074 galaxies, 1455 have *XMM–Newton* data in the archive. Therefore, the likelihood of seeing such a chance alignment in the *XMM–Newton* data which is unresolved by the NVSS data is 1.37×10^{-4} multiplied by 1455, yielding a value of ∼0.2.

To test the possibility that three X-ray sources could align on the sky within 3 arcmin, purely from random chance, we ran simulations. Within a 3 arcmin box, we placed three points in uniformly random positions many times. For each iteration, we estimated whether all three sources were aligned with the central source at the origin. To perform this step, we traced out an area from the origin given by the width of the central source (30 arcsec in the case of NGC 6217) projected along the line of the closest source to the origin, out to the edge of the 3 arcmin box. If all of the three points were found in this error region, we considered them aligned. We then ran enough iterations that additional runs resulted in negligible statistical improvement. We found that the probability of three knots aligning is ∼0.3 per cent, which is fully consistent with our probabilistic estimate from the *XMM–Newton* source counts.

A more detailed, simulation-based, analysis would be needed to put uncertainties on both our estimated probability values, but variation by greater than a factor of 2, either way, is unlikely. Thus, we cannot rule out the null hypothesis that the alignment is just a chance coincidence. Furthermore, these values should be treated as an upper limit since we do not consider the probability that the spectra, fluxes, and hardness ratios (see F17) are similar among the knots.

4.2.2 The nature of the X-ray knots

We now consider the three X-ray knots in turn and attempt to explain plausible origins for these X-ray knots, given the lack of cospatial radio emission and multiwavelength associations. From the extracted optical–IR sources associated with the X-ray knots within the 21 arcsec X-ray extraction region, we built up their SEDs (see Section 3.2 and Table [4]). The genuine physical relation between the X-ray and optical–IR associations goes beyond our reasonable attempt to investigate the nature of these knots. Therefore, caution needs to be taken when considering the physical properties derived for these sources.

Concerning the multiband identifications of knot 1, two *Spitzer* sources fall within the 21 arcsec X-ray extraction region. The SED fit for the source nearest to the X-ray knot is limited by the lack of data points. However, we calculate a photometric redshift of $0.48^{+0.25}_{-0.12}$ with a bolometric luminosity of 7.9×10^{43} erg s^{-1} for this source. We also extracted the SED of the other *Spitzer* source found in the extraction region of knot 1. This source is detected in SDSS *r*, *i*, and *z* as well as all the IR bands and we found a photometric redshift of $0.49^{+0.16}_{-0.13}$, consistent with the former *Spitzer* source. Given these similar redshifts and their proximity to one another, their separation can be estimated to be of order of 100 kpc and hence may be part of a cluster of galaxies.

Similar to knot 1, two *Spitzer* sources fall within the X-ray spectral extraction radius of knot 2, but unlike knot 1, one of the two *Spitzer* sources well matches the centroid of X-ray knot 2 within 0.5 arcsec. This *Spitzer* source also has SDSS and *WISE* detections, as well as an *HST* detection. This cospatiality increases the probability that the X-ray knot and the optical–IR associations are physically related. It should be noted that the optical/IR detections described here are not related to the background star mentioned in F17, 1.6 arcsec away from the knot. The optical–IR SED fit requires the inclusion of the spectrum of a Seyfert-like AGN with strong emission lines which constrains its photo-*z* at $0.70^{+0.03}_{-0.02}$ with a bolometric luminosity of 8.3×10^{43} erg s^{-1}.

Finally, X-ray knot 3 has a complicated X-ray morphology, with two distinct X-ray blobs in the X-ray extraction region. There is a *Spitzer* source coincident with the western X-ray component in this knot (see Fig. [2]), which is also coincident with the extended SDSS

source discussed by F17 and an *HST* source that F17 attributed to an unrelated galaxy. Assuming that the optical–IR associations are related to the emission of the knot 3, we modelled the SED with a young and old stellar population with a photo-z of $0.46^{+0.19}_{-0.06}$ and a bolometric luminosity of 9.3×10^{43} erg s^{-1}. This tentative multiband identification of the X-ray emission from knot 3 makes the nature of this knot as a background source questionable.

Although caution on the interpretation of these knots is needed, the multiband associations found for the X-ray knots may suggest an extragalactic background origin for these components. This interpretation is supported by the large inferred X-ray and bolometric luminosities (see Table 4, $\sim 10^{43}$ erg s^{-1}, assuming the photo-z are correct) and X-ray photon indices consistent with an AGN origin (Nandra & Pounds 1994; Reeves & Turner 2000; Piconcelli et al. 2005; Page et al. 2005; Ishibashi & Courvoisier 2010). Specifically, the ratio between the limits on the radio and X-ray luminosities are similar to those found in Seyfert galaxies and other low-luminosity AGN (e.g. Panessa et al. 2007; Laor & Behar 2008). However, in the case that the sources belong to the host galaxy, NGC 6217, all of the knots would have luminosities ($\sim 10^{39}$ erg s^{-1}), which could be consistent with different types of source, such as XRBs or being part of a jet. Therefore, we cannot put firm conclusions on the nature of any of these multiwavelength associations to the X-ray knots. Further high-resolution data with *Chandra* will greatly improve our understanding of these sources, by providing higher angular and spectral resolution data which will allow for true X-ray counterparts to be found for each of the associations.

4.3 Radio emission from secondary sources in NGC 6217

For the sources that were within the optical extent of the galaxy (panels B and C in Fig 2), we did not attempt to extract their SEDs or look for X-ray emission because emission from the galaxy would confuse the SED fits and the *XMM–Newton* data are not of sufficient resolution to identify these objects separately. Both sources have e-MERLIN flux densities of $\lesssim 5$ mJy at a size of 0.15 arcsec $\times$ 0.15 arcsec, and therefore have brightness temperatures too low to claim a clear AGN activity. However, these do not align with the star-forming regions found by Gusev et al. (2012, 2016) in NGC 6217. The source found in the spiral arms (panel B in Fig. 2) shows an extended structure and is co-incident with a 3σ *Spitzer* source. Judging from the radio emission alone, these radio sources are possibly either H II regions or background AGN. Additional high-resolution X-ray data would help in to identify these sources.

The radio source located between the X-ray knots 1 and 2 (panel D) is associated with a weak *Spitzer* source (R). Modelling the only detected IR part of its SED provides an inconclusive photo-z of $0.19^{+0.25}_{-0.12}$ with a bolometric luminosity of 4.6×10^{42} erg s^{-1}. This source appears compact and unresolved at e-MERLIN and VLA A-Array baseline scales, with similar flux density values and appears unrelated to the X-ray emission of the contiguous knots. The most simple interpretation of this source is a background galaxy associated with a low-luminosity radio AGN, with a radio structure confined in a kpc scale. This scenario is in line with the population of compact radio galaxies (named FR 0s, Baldi, Capetti & Giovannini 2015; Baldi, Capetti & Massaro 2018b) found in the local Universe. In addition, it also likely that this radio source contributes to the radio elongation observed in NVSS at larger beam sizes along the putative X-ray jet.

5 CONCLUSIONS

We analysed new high-resolution radio interferometric data of the barred spiral galaxy NGC 6217 with the high angular resolution and sensitivity of e-MERLIN. For the first time, we have resolved the nuclear region of NGC 6217, which consists of two radio lobes projected north-west to south-east. The nuclear morphology is similar to CSS or GPS sources (Orienti 2016) but shows no core component. Starburst superwinds have been observed to show similar morphologies, but usually oriented along the minor axis of the galaxy (Ulvestad & Wilson 1984; Kinney et al. 2000; Gallimore et al. 2006). The *XMM–Newton* X-ray spectra suggest a good fit (χ^2/d.o.f. ~ 1) for an absorbed power law, with an additional thermal component. The energetics, optical line ratios, and radio brightness temperature of the core region cannot rule out SF as the main contributor to the emission, but are also consistent with an LLAGN emission origin. Given the radio morphology, X-ray spectra and lack of alignment with the galaxy minor axis, we conclude that the nuclear region is most likely powered by an LLAGN, probably with a LINER-type nucleus, with multiband contamination from SF or other nuclear X-ray sources. Therefore, the 400-pc twin-lobed structure of NGC 6217 constitutes one of the smallest radio structures observed in the nuclei of nearby LLAGN. To confirm the emission mechanism, further high-resolution X-ray data (e.g. *Chandra*) and optical (photometry and spectroscopy from *HST*) data are needed.

The 'putative' X-ray jet in NGC 6217 is not coincident with any radio emission observed with e-MERLIN or the VLA at 1.51 GHz. Furthermore, the extension of the nuclear radio bubble is oriented almost perpendicular to the putative X-ray jet. We therefore reconsidered the background source origin of the X-ray knots as we found multiband sources co-incident within the X-ray spectral extraction regions. By extracting photometry of all these sources in the optical/IR bands, we performed SED fits and found that all of the X-ray 'knots' were plausibly consistent with higher redshift ($\gtrsim 0.4$) sources such as background AGN and galaxies and therefore likely not belonging to NGC 6217. However, the sparse multiband coverage of the SEDs of the X-ray knots does not ensure the correctness of the physical parameters inferred for these knots and therefore we cannot come to a definite conclusion on the nature of these sources as they are intrinsically faint. Furthermore, due to the high source density of *Spitzer* sources expected in the spectral extraction regions, it is possible that these IR sources are chance associations with the X-ray 'knots'. We calculated that the likelihood of the 'knots' aligning in such a way to be $P = 0.2$ based on *XMM–Newton* integral source counts. By simulating aligned sources in random positions in a square field equal to the length of the X-ray 'knot' structure, we found that such alignments occur in 0.3 per cent of cases. Thus, we cannot rule out the null hypothesis that the alignment is just a chance coincidence. Therefore, these X-ray knots would benefit from higher resolution X-ray data to confirm their optical/IR associations. However, given that there are no radio associations to the X-ray knots, we have shown that the X-ray jet hypothesis is unlikely in this source.

We also investigated the other radio components observed in the new high-resolution images of NGC 6217. We found a radio source that coincidentally aligned along the PA of the putative X-ray jet, but not associated with any of the X-ray emission. We suggest that this may be due to a background radio AGN of redshift ~ 0.19. The two other sources of radio emission are possibly H II regions in the galaxy or background AGN, but additional data are required to test this hypothesis.

The study of radio emission in the nuclear regions of nearby LLAGN is important for discriminating SF from AGN activity. Our observations of NGC 6217 show that such studies can only be undertaken with the unique combination of good angular and spectral resolution provided by e-MERLIN. By combining e-MERLIN data with the VLA, it is possible to probe multiple spatial scales simultaneously. However, understanding how nuclear regions of nearby galaxies are ionized, whether by an LLAGN of SF, is only possible by comparing radio data with high-resolution optical and X-ray data. Furthermore, the LeMMINGs sample allows for such studies to be undertaken in a statistically complete way to compare the different radio morphologies across all nuclear optical classifications.

REFERENCES

Arnaud K. A., 1996, in Jacoby G. H., Barnes J., eds, ASP Conf. Ser. Vol. 101, Astronomical Data Analysis Software and Systems V. Astron. Soc. Pac., San Francisco, p. 17

Bagchi J., Gopal-Krishna, Krause M., Joshi S., 2007, ApJ, 670, L85

Baldi R. D. et al., 2018a, MNRAS, 476, 3478

Baldi R. D., Chiaberge M., Capetti A., Rodriguez-Zaurin J., Deustua S., Sparks W. B., 2013, ApJ, 762, 30

Baldi R. D., Capetti A., Chiaberge M., Celotti A., 2014, A&A, 567, A76

Baldi R. D., Capetti A., Giovannini G., 2015, A&A, 576, A38

Baldi R. D., Capetti A., Massaro F., 2018b, A&A, 609, A1

Baldwin J. A., Phillips M. M., Terlevich R., 1981, PASP, 93, 5

Baum S. A., O'Dea C. P., Dallacassa D., de Bruyn A. G., Pedlar A., 1993, ApJ, 419, 553

Belles P.-E., Beswick R., Argo M., Jackson N., Muxlow T., Richards A., 2015, e-MERLIN CookBook – version 3.0, 2015 February. JBCA.

Beswick R., Argo M. K., Evans R., McHardy I., Williams D. R. A., Westcott J., 2014, in Proceedings of the 12th European VLBI Network Symposium and Users Meeting (EVN' 14). Cagliari, Italy, p. 10

Bonzini M., Padovani P., Mainieri V., Kellermann K. I., Miller N., Rosati P., Tozzi P., Vattakunnel S., 2013, MNRAS, 436, 3759

Bruzual G., Charlot S., 2011, Astrophysics Source Code Library, record ascl:1104.005

Buta R. J. et al., 2015, ApJS, 217, 32

Buttiglione S., Capetti A., Celotti A., Axon D. J., Chiaberge M., Macchetto F. D., Sparks W. B., 2010, A&A, 509, A6

Cabrera-Lavers A., Garzón F., 2004, AJ, 127, 1386

Calzetti D., Armus L., Bohlin R. C., Kinney A. L., Koornneef J., Storchi-Bergmann T., 2000, ApJ, 533, 682

Capetti A., Baldi R. D., 2011, A&A, 529, A126

Capetti A., Balmaverde B., 2010, Astrophys. Space Sci. Proc., 15, 175

Capetti A., Massaro F., Baldi R. D., 2017, A&A, 598, A49

Cash W., 1979, ApJ, 228, 939

Celotti A., Ghisellini G., Chiaberge M., 2001, MNRAS, 321, L1

Chartas G. et al., 2000, ApJ, 542, 655

Chiaberge M., Gilli R., Capetti A., Macchetto F. D., 2003, ApJ, 597, 166

Cirasuolo M., Magliocchetti M., Celotti A., Danese L., 2003, MNRAS, 341, 993

Colbert E. J. M., Baum S. A., Gallimore J. F., O'Dea C. P., Christensen J. A., 1996, ApJ, 467, 551

Comerón S., Knapen J. H., Beckman J. E., Laurikainen E., Salo H., Martínez-Valpuesta I., Buta R. J., 2010, MNRAS, 402, 2462

Condon J. J., 1987, ApJS, 65, 485

Condon J. J., 1992, ARA&A, 30, 575

Condon J. J., Helou G., Sanders D. B., Soifer B. T., 1990, ApJS, 73, 359

Congiu E. et al., 2017, A&A, 603, A32

de Vaucouleurs G., de Vaucouleurs A., Corwin Jr. H. G., Buta R. J., Paturel G., Fouqué P., 1991, Third Reference Catalogue of Bright Galaxies. Volume I: Explanations and References. Volume II: Data for Galaxies between 0^h and 12^h. Volume III: Data for Galaxies between 12^h and 24^h, Springer, New York.

Dullo B. T. et al., 2018, MNRAS, 475, 4670

Dullo B. T., Martínez-Lombilla C., Knapen J. H., 2016, MNRAS, 462, 3800

Elmouttie E., Haynes R. F., Jones K. L., Ehle M., Beck R., Wielebinski R., 1995, MNRAS, 275, L53

Elmouttie M., Haynes R. F., Jones K. L., Sadler E. M., Ehle M., 1998, MNRAS, 297, 1202

Falocco S., Larsson J., Nandi S., 2017, MNRAS, 472, 2280(F17)

Ferland G. J., Netzer H., 1983, ApJ, 264, 105

Ferrarese L., Merritt D., 2000, ApJ, 539, L9

Filippenko A. V., Sargent W. L. W., 1985, ApJS, 57, 503

Francis P. J., Hewett P. C., Foltz C. B., Chaffee F. H., Weymann R. J., Morris S. L., 1991, ApJ, 373, 465

Gallimore J. F., Axon D. J., O'Dea C. P., Baum S. A., Pedlar A., 2006, AJ, 132, 546

Gusev A. S. et al., 2016, MNRAS, 457, 3334

Gusev A. S., Pilyugin L. S., Sakhibov F., Dodonov S. N., Ezhkova O. V., Khramtsova M. S., 2012, MNRAS, 424, 1930

Halpern J. P., Steiner J. E., 1983, ApJ, 269, L37

Hardcastle M. J., Worrall D. M., Kraft R. P., Forman W. R., Jones C., Murray S. S., 2003, ApJ, 593, 169

Hardcastle M. J., Croston J. H., Kraft R. P., 2007, ApJ, 669, 893

Hardcastle M. J., Evans D. A., Croston J. H., 2009, MNRAS, 396, 1929

Harris D. E. et al., 2017, ApJ, 846, 119

Harris D. E., Krawczynski H., 2006, ARA&A, 44, 463

Heckman T. M., 1980, A&A, 87, 152

Heckman T. M., Lehnert M. D., Armus L., 1993, in Shull J. M., Thronson H. A., eds, Astrophysics and Space Science Library Vol. 188, The Environment and Evolution of Galaxies. Kluwer, Dordrecht, p. 455

Heesen V., Beck R., Krause M., Dettmar R.-J., 2009, A&A, 494, 563

Hlavacek-Larrondo J. et al., 2017, MNRAS, 464, 2223

Hocuk S., Barthel P. D., 2010, A&A, 523, A9

Hopkins P. F., Richards G. T., Hernquist L., 2007, ApJ, 654, 731

Hota A., Saikia D. J., 2006, MNRAS, 371, 945

Ho L. C., Ulvestad J. S., 2001, ApJS, 133, 77

Ho L. C., Filippenko A. V., Sargent W. L., 1995, ApJS, 98, 477

Ho L. C., Filippenko A. V., Sargent W. L. W., 1997a, ApJS, 112, 315

Ho L. C., Filippenko A. V., Sargent W. L. W., Peng C. Y., 1997b, ApJS, 112, 391

Ho L. C., Filippenko A. V., Sargent W. L. W., Peng C. Y., 1997c, ApJS, 112, 391

Ho L. C., Filippenko A. V., Sargent W. L. W., 1997d, ApJ, 487, 568

Ho L. C., Filippenko A. V., Sargent W. L. W., 1997e, ApJ, 487, 591

Ho L. C., Filippenko A. V., Sargent W. L. W., 2003, ApJ, 583, 159

Ho L. C., Greene J. E., Filippenko A. V., Sargent W. L. W., 2009, ApJS, 183, 1

Hummel E., 1980, A&AS, 41, 151

Hummel E., Pedlar A., Davies R. D., van der Hulst J. M., 1985, A&AS, 60, 293

Irwin J. A. et al., 2017, MNRAS, 464, 1333

Irwin J. A., Saikia D. J., 2003, MNRAS, 346, 977

Ishibashi W., Courvoisier T. J.-L., 2010, A&A, 512, A58

James P. A. et al., 2004, A&A, 414, 23

Jester S., Röser H.-J., Meisenheimer K., Perley R., 2005, A&A, 431, 477

Kalberla P. M. W., Burton W. B., Hartmann D., Arnal E. M., Bajaja E., Morras R., Pöppel W. G. L., 2005, A&A, 440, 775

Kellermann K. I., Sramek R., Schmidt M., Shaffer D. B., Green R., 1989, AJ, 98, 1195

Kewley L. J., Dopita M. A., Sutherland R. S., Heisler C. A., Trevena J., 2001, ApJ, 556, 121

Kewley L. J., Groves B., Kauffmann G., Heckman T., 2006, MNRAS, 372, 961

Kharb P. et al., 2012, AJ, 143, 78

Kharb P., O'Dea C. P., Baum S. A., Colbert E. J. M., Xu C., 2006, ApJ, 652, 177

Kharb P., Hota A., Croston J. H., Hardcastle M. J., O'Dea C. P., Kraft R. P., Axon D. J., Robinson A., 2010, ApJ, 723, 580

Kharb P., Lal D. V., Merritt D., 2017, Nat. Astron., 1, 727

Kinney A. L., Schmitt H. R., Clarke C. J., Pringle J. E., Ulvestad J. S., Antonucci R. R. J., 2000, ApJ, 537, 152

Knapen J. H., James P. A., 2009, ApJ, 698, 1437

Knapen J. H., Stedman S., Bramich D. M., Folkes S. L., Bradley T. R., 2004, A&A, 426, 1135

Kraft R. P., Forman W. R., Jones C., Murray S. S., Hardcastle M. J., Worrall D. M., 2002, ApJ, 569, 54

Kukula M. J., Ghosh T., Pedlar A., Schilizzi R. T., 1999, ApJ, 518, 117

Laor A., Behar E., 2008, MNRAS, 390, 847

Magorrian J. et al., 1998, AJ, 115, 2285

Marshall H. L., Miller B. P., Davis D. S., Perlman E. S., Wise M., Canizares C. R., Harris D. E., 2002, ApJ, 564, 683

McMullin J. P., Waters B., Schiebel D., Young W., Golap K., 2007, in Shaw R. A., Hill F., Bell D. J., eds, ASP Conf. Ser. Vol. 376, Astronomical Data Analysis Software and Systems XVI, Astron. Soc. Pac., San Francisco. p. 127

Meyer E. T., Breiding P., Georganopoulos M., Oteo I., Zwaan M. A., Laing R., Godfrey L., Ivison R. J., 2017, ApJ, 835, L35

Mingo B. et al., 2016, MNRAS, 462, 2631

Muxlow T. W. B. et al., 2010, MNRAS, 404, L109

Nandra K., Pounds K. A., 1994, MNRAS, 268, 405

Nicholson K. L., Mittaz J. P. D., Mason K. O., 1997, MNRAS, 285, 831

Nyland K. et al., 2017, ApJ, 845, 50

Orienti M., 2016, Astron. Nachr., 337, 9

Pacholczyk A. G., Scott J. S., 1976, ApJ, 203, 313

Padovani P. et al., 2017, A&AR, 25, 2

Padovani P., 2017, Nat. Astron., 1, 0194

Page K. L., Reeves J. N., O'Brien P. T., Turner M. J. L., 2005, MNRAS, 364, 195

Panessa F., Barcons X., Bassani L., Cappi M., Carrera F. J., Ho L. C., Pellegrini S., 2007, A&A, 467, 519

Panessa F., Baldi R. D., Laor A., Padovani P., Behar E., McHardy I., 2019, Nat. Astron., 3, 387

Paturel G., Petit C., Prugniel P., Theureau G., Rousseau J., Brouty M., Dubois P., Cambrésy L., 2003, A&A, 412, 45

Peck L. W., Fenech D. M., 2013, Astron. Comput., 2, 54

Pedlar A., Unger S. W., Dyson J. E., 1985, MNRAS, 214, 463

Piconcelli E., Jimenez-Bailón E., Guainazzi M., Schartel N., Rodríguez-Pascual P. M., Santos-Lleó M., 2005, A&A, , 432, 15

Pietsch W., Arp H., 2001, A&A, 376, 393(PA01)

Planck Collaboration et al., 2014, A&A, 571, A16

Ramírez-Olivencia N. et al., 2018, A&A, 610, L18

Rampadarath H. et al., 2018, MNRAS, 476, 2876

Ranalli P. et al., 2013, A&A, 555, A42

Reeves J. N., Turner M. J. L., 2000, MNRAS, 316, 234

Robitaille T. P., Rossa J., Bomans D. J., van der Marel R. P., 2007, A&A, 464, 541

Ruiz A., Miniutti G., Panessa F., Carrera F. J., 2010, A&A, 515, A99

Saikia P., Körding E., Falcke H., 2015, MNRAS, 450, 2317

Saikia P., K örding E., Dibi S., 2018, MNRAS, 477, 2119
Sambruna R. M., Urry C. M., Tavecchio F., Maraschi L., Scarpa R., Chartas G., Muxlow T., 2001, ApJ, 549, L161
Sánchez-Gallego J. R., Knapen J. H., Wilson C. D., Barmby P., Azimlu M., Courteau S., 2012, MNRAS, 422, 3208
Sandage A., Tammann G. A., 1981, in A Revised Shapley-Ames Catalog of Bright Galaxies, Carnegie Institution, Washington, p. 635
Schwartz D. A. et al., 2000, ApJ, 540, 69
Sheth K. et al., 2010, PASP, 122, 1397
Simionescu A. et al., 2016, ApJ, 816, L15
Singh R. et al., 2013, A&A, 558, A43
Stobbart A.-M., Roberts T. P., Wilms J., 2006, MNRAS, 368, 397
Tavecchio F., Maraschi L., Sambruna R. M., Urry C. M., 2000, ApJ, 544, L23
Terashima Y., Wilson A. S., 2003, ApJ, 583, 145
Terlevich R., Melnick J., 1985, MNRAS, 213, 841
Torresi E., Grandi P., Capetti A., Baldi R. D., Giovannini G., 2018, MNRAS, 476, 5535
Tully R. B., Fisher J. R., 1977, A&A, 54, 661

Tutui Y., Sofue Y., 1997, A&A, 326, 915
Ulvestad J. S., Wilson A. S., 1984, ApJ, 285, 439
van Driel W., Buta R. J., 1991, A&A, 245, 7
Véron-Cetty M.-P., Véron P., 2006, A&A, 455, 773
Vila M. B., Pedlar A., Davies R. D., Hummel E., Axon D. J., 1990, MNRAS, 242, 379
Wells D. C., 1985, Data Analysis in Astronomy. Springer, Boston, MA
Westcott J. et al., 2017, MNRAS, 467, 2113,
Williams D. R. A. et al., 2017, MNRAS, 472, 3842
Wilson A. S., Ulvestad J. S., 1983, ApJ, 275, 8
Wilson A. S., Yang Y., 2002, ApJ, 568, 133
Woo J.-H., Urry C. M., 2002, ApJ, 579, 530
Worrall D. M., 2009, A&AR, 17, 1
Wright E. L. et al., 2010, AJ, 140, 1868

This paper has been typeset from a TEX/LATEX file prepared by the author.